AMPHIBOLE IN ULTRA-DEPLETED PERIDOTITES FROM THE HOROKANAI OPHIOLITE, HOKKAIDO, JAPAN: BONINITE MELT TRAPPED IN THE MANTLE WEDGE

Akihiro Tamura*,✉, Ikuya Nishio*,, Yuya Iwata*, Shoji Arai*** and **Tomoaki Morishita*,*****

* *Department of Earth Sciences, Kanazawa University, Japan.*
** *Department of Geosciences and Natural Resource Management, University of Copenhagen, Denmark.*
*** *Research Institute for Marine Geodynamics, Japan Agency for Marine-Earth Sciences and Technology, Yokosuka, Japan.*
✉ *Corresponding author, email: aking826@gmail.com*

Keywords: *harzburgite; pargasite; hydrous melting; boninite; mantle wedge.*

ABSTRACT

Ultra-depleted peridotites have been reported from the mantle sections of a number of ophiolitic complexes (e.g., Papua New Guinea and New Caledonia). Such rocks are residues derived from boninitic melts in supra-subduction zones, particularly in forearcs. In the mantle wedge, slab-derived fluid-melt containing H_2O increases the degree of melting and metasomatizes the peridotites. However, the relationship between high-degree melting under hydrous conditions and metasomatism is not well understood. In this paper, we report petrological features of amphibole-bearing ultra-depleted peridotites from the Horokanai ophiolite, Hokkaido, Japan. The peridotite complex in the Horokanai ophiolite consists of clinopyroxene-free harzburgite, orthopyroxene-poor harzburgite, and dunite. The harzburgites contain high-Cr# spinel (0.70-0.85) and orthopyroxene with very low abundances of incompatible elements (e.g., Y < 0.01 μg/g; Ti ~ 2 μg/g). Pargasitic-edenitic amphibole occurs as spinel-hosted inclusions and as an interstitial phase to olivine and orthopyroxene. The harzburgite is a residue formed by the high-degree melting caused by fluid flux. The hydrous conditions cause incongruent melting of orthopyroxene, producing a depleted Si-rich melt (i.e., a boninitic melt). Because such Si-rich melt can coexist with Cr-rich spinel under these conditions, amphibole is ultimately crystallized in the harzburgite. Such amphibole formation is important in producing secondary sodic amphibole during alteration of ultra-depleted peridotites.

INTRODUCTION

Petrological and geochemical studies of abyssal peridotites have contributed to our understanding of magmatism at mid-ocean ridges where oceanic lithosphere is created. Abyssal peridotites represent residual mantle after the generation of mid-ocean ridge basalt (MORB) melt by fractional melting. The melting degree does not exceed 15%, as inferred by melting models using incompatible elements in clinopyroxene (e.g., Johnson et al., 1990; Warren et al., 2016). The Cr# [Cr/(Cr + Al) atomic ratio] of spinel is also a good indicator of the degree of melting and rarely exceeds 0.4 in abyssal peridotites (Arai, 1987; 1994a; Hellebrand et al., 2001). In contrast, highly depleted peridotites with spinel Cr# > 0.4 have commonly been reported from ophiolitic complexes (Le Roux et al., 2014; Jean and Shervais, 2017) and from forearc regions of the western Pacific (e.g., Parkinson and Pearce, 1998; Birner et al., 2017). Moreover, ultra-depleted peridotites with spinel Cr# > 0.7 have been identified in Papua New Guinea and New Caledonia ophiolites (e.g., Jaques and Chappell, 1980; Xu et al., 2021; Barret et al., 2022).

In general, studies of ultra-depleted peridotites cannot obtain incompatible element compositions of clinopyroxene because of the absence of this mineral in such samples. However, trace-element data for orthopyroxene have been reported for harzburgites (e.g., Parkinson and Pearce, 1998; Ishimaru et al., 2007; Scott et al., 2016; Jean and Shervais, 2017). Despite the low abundances of incompatible elements, elemental data for orthopyroxene allow the melting of clinopyroxene-free harzburgite to be investigated by quantitative modeling (Scott et al., 2016; Nishio et al., 2023).

Highly depleted peridotites are probably derived from the mantle beneath arcs, such as from the mantle wedge. Hydrous melts and/or aqueous fluids derived from a subducted slab increase the degree of melting of peridotite (e.g., Tatsumi et al., 1983). In fact, such peridotites are exposed at the landward slope of the trench at convergent margins (e.g., Birner et al., 2022). Therefore, their origins provide key evidence for magmatic processes in the mantle wedge and particularly the generation of boninites in the forearc (Pearce et al., 1992). König et al. (2010) and Cluzel et al. (2016) showed that slab-derived melt-fluid have an important role in the generation of boninitic magma during melting of the mantle wedge. Several studies have investigated the lithological and/or geochemical signatures of boninitic magmas in the mantle, including dunite, pyroxenite, and chromitite in harzburgite, and discussed the relationship between boninites and these lithologies (e.g., Varfalvy et al., 1996; Suhr et al., 2003; Tamura and Arai, 2006a; Xu et al., 2021).

Amphibole-bearing peridotite xenoliths in arc volcanic rocks reflect the hydrous conditions in the mantle wedge (e.g., Grégoire et al., 2001; Ishimaru and Arai, 2008; Ionov, 2010). Mantle metasomatism is caused by slab-derived melt-fluid and produces hydrous mantle peridotites. Melting of such metasomatized peridotites may produce highly depleted peridotites under hydrous conditions in the mantle wedge (e.g., Pearce et al., 1992). Amphiboles have also been reported in highly depleted peridotites from ophiolites and trenches (e.g., Ozawa, 1988; Ohara and Ishii, 1998; Ichiyama et al., 2021). However, it is difficult to constrain the origins of the amphibole, because amphibole can be formed by alteration by aqueous fluids after melting. Therefore, the relationship between hydrous melting and the high degree of melting has not been examined in detail, even for amphibole-bearing peridotites.

Highly depleted peridotite complexes occur in the Kamuikotan zone in Hokkaido, Japan (e.g., Katoh and Nakagawa, 1986; Tamura et al., 1999a, 1999b; Kubo, 2002). Two

peridotite complexes comprising the mantle section of the Horokanai ophiolite are extremely depleted, and the peridotites are characterized by their absence of clinopyroxene and high spinel Cr# (> 0.7) (e.g., Igarashi et al., 1985; Ishizuka, 1985; Tamura et al., 1999a; 1999b; Nishio et al., 2023). This paper presents petrological and geochemical features of pargasitic amphibole-bearing harzburgite from the Horokanai ophiolite. We demonstrate that these rocks are ultra-depleted peridotites, and discuss that the amphibole is derived from a partial melt related to the generation of boninitic melt in the mantle wedge.

GEOLOGICAL AND PETROLOGICAL BACKGROUND

Several serpentinized peridotite bodies are distributed in the Kamuikotan zone, Hokkaido, Japan (Fig. 1a) (Katoh and Nakagawa, 1986). The Kamuikotan zone extends from north to south for a length of 320 km and width of 25 km in the central axial zone of Hokkaido and consists mainly of subduction-related high-pressure and low-temperature (high-P/T) metamorphic rocks. The Kamuikotan zone belongs to the Sorachi-Yezo belt, which comprises a Cretaceous forearc basin and accretionary sediments (Sakakibara and Ota, 1994; Wallis et al., 2020). The petrological features of peridotites in the Kamuikotan zone are variable and characterized by an increasing degree of melting from south to north (Katoh and Nakagawa, 1986; Tamura and Arai, 2006b). Highly depleted peridotites occur in the Iwanai-dake complex and the Horokanai area (Igarashi et al., 1985; Ishizuka, 1985; Kubo, 2002; Tamura and Arai, 2005).

Ophiolitic rocks are exposed in the Horokanai area in northern Hokkaido (i.e., the Horokanai ophiolite; Fig. 1b; Asahina and Komatsu, 1979; Ishizuka, 1987). Pillow lavas and volcanic complexes underlying radiolarian cherts in the ophiolite sequences have mid-ocean ridge basalt (MORB)-like geochemical features and have undergone ocean-floor metamorphism (i.e., low-P metamorphism; Ishizuka et al., 1983). In the lower crustal section, depleted ultramafic rocks are characterized by orthopyroxenite-dunite layers below amphibolite and gabbro (Fig. 1c) (Ishizuka, 1985). Two peridotite bodies (i.e., the Horokanai and Takadomari complexes) are exposed in the mantle section of the Horokanai ophiolite (Fig. 1b; Igarashi et al., 1985; Ishizuka, 1985). Both peridotite complexes consist mainly of clinopyroxene-free harzburgite and dunite. These ultra-depleted peridotites have spinel Cr# > 0.7 (Ishizuka, 1985; Katoh and Nakagawa, 1986; Tamura et al., 1999a; 1999b; Nishio et al., 2023). Although they are depleted, these compositional features are similar to those of peridotites from the forearc region (e.g., Parkinson and Pearce, 1998). Ishizuka (1980) reported the presence of sodic tremolite in dunite from the Horokanai complex. In addition, a Cr-Na-rich amphibole-bearing rock (chromian richterite rock) has also been discovered (Ishii et al., 2002).

SAMPLE PETROGRAPHY AND MINERAL CHEMISTRY

The studied harzburgite and dunite samples were collected from Mamusi-no-sawa in the Horokanai complex (Fig. 1). The harzburgite samples consist of olivine, orthopyroxene, and spinel and contain no clinopyroxene (Fig. 2). The orthopyroxene content is as low as 5-15 vol.% in the harzburgites and very low (< 1 vol.%) in dunite. The subhedral-anhedral orthopyroxene is ~ 5 mm in size (Fig. 2a). Fine-grained (< 1 mm) anhedral orthopyroxene occurs in the harzburgites and dunite (Fig. 2b-d). The peridotites are severely serpentinized. Orthopyroxene is partly replaced by bastite, which is distinguishable from olivine altered to serpentine (Fig. 2b).

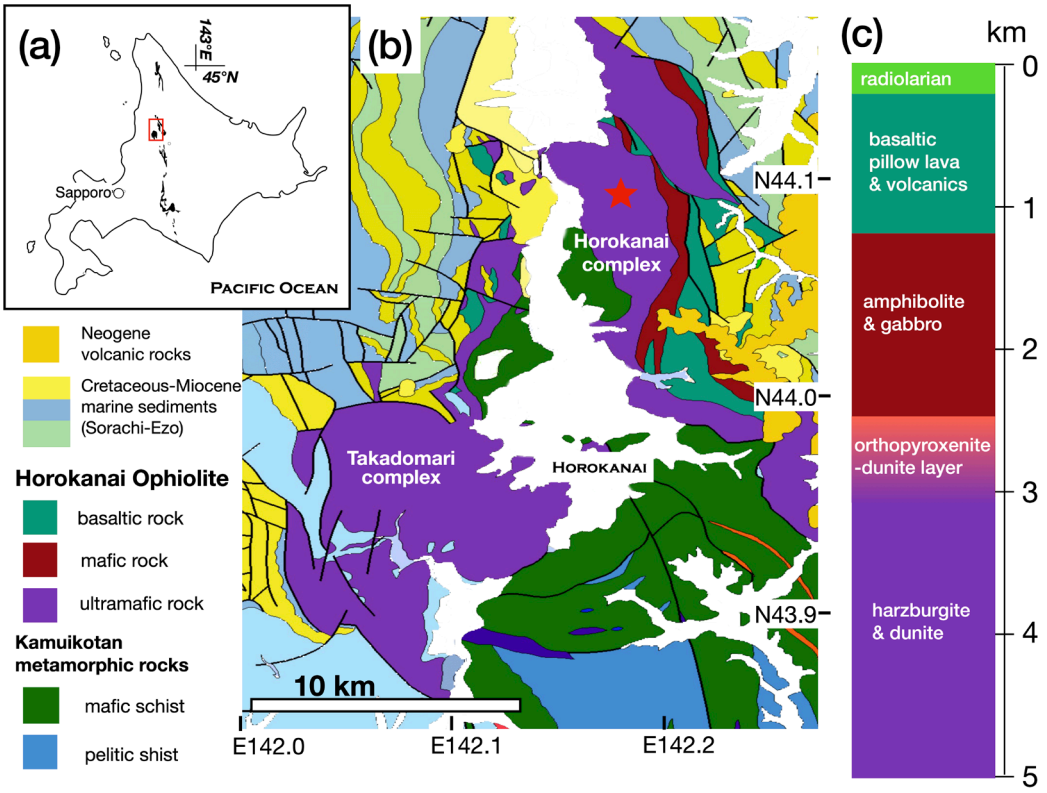

Fig. 1 - (a) Distribution of the ultramafic complexes in the Kamuikotan zone, Hokkaido Island, Japan. (b) Geological map of the Horokanai area (modified from the geological map of the Geological Survey of Japan; https://gbank.gsj.jp/geonavi/) and locations of the studied samples (star symbols). Two ultramafic complexes contain mantle sections of the Horokanai ophiolite (Horokanai and Takadomari complexes). (c) Schematic section of the Horokanai ophiolite (modified after Ishizuka, 1985).

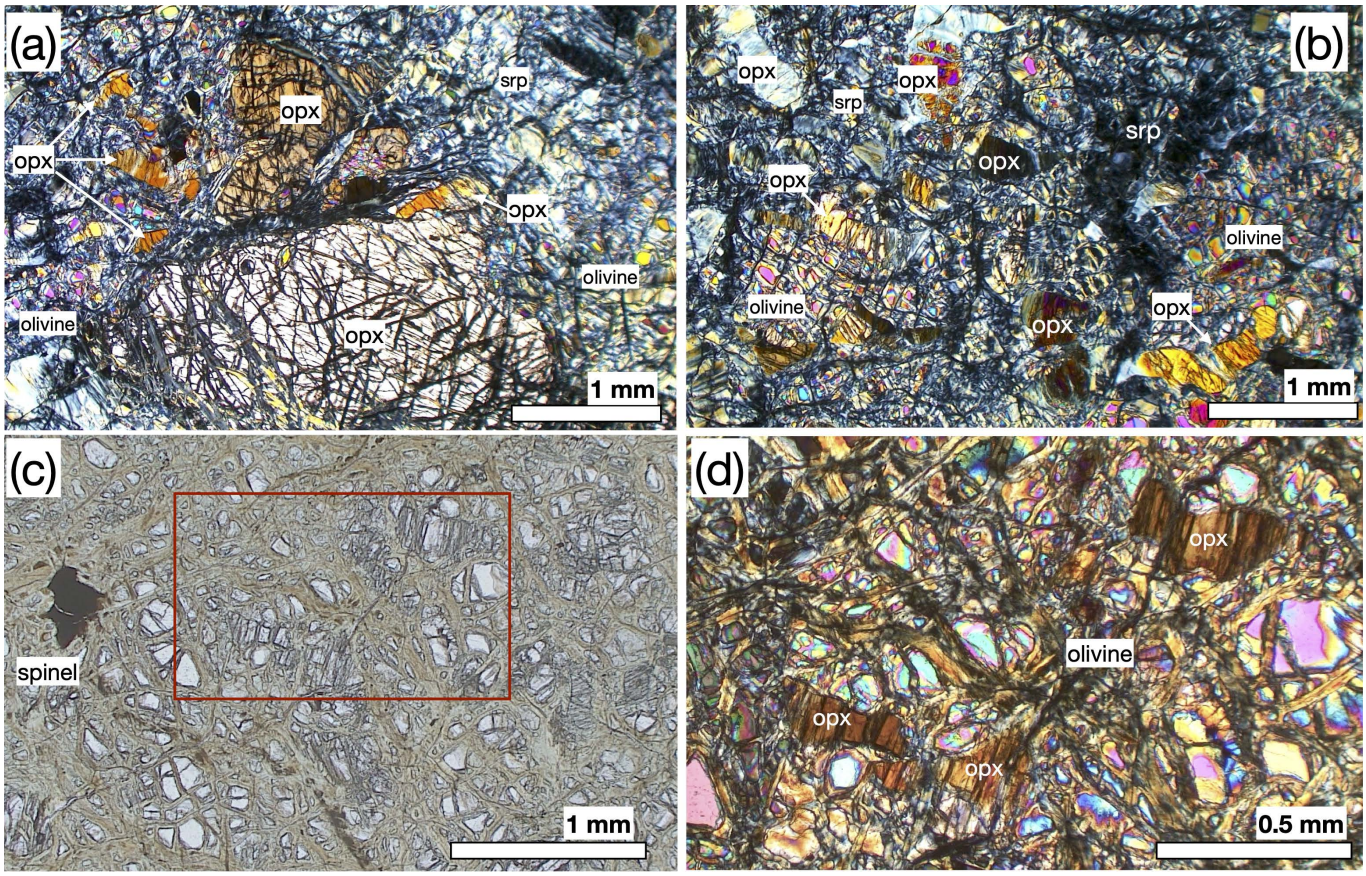

Fig. 2 - Photomicrograph of (a-b) harzburgite (#91501) and (c-d) orthopyroxene-poor harzburgite (d1harz) from the Horokanai complex (cross-polarized light except c). (a) Coarse- and fine-grained orthopyroxene. (b) Anhedral or interstitial fine-grained orthopyroxene. Orthopyroxene is locally partly replaced by bastite. (c) Anhedral spinel and fine-grained orthopyroxene in olivine and serpentine (plane-polarized light). (d) Enlarged view of the area in the red square in (c). Opx, Orthopyroxene; Srp, Serpentine.

Green amphibole is present in one harzburgite sample (#91502; Fig. 3) and is classified as chromio-pargasite according to the nomenclature of Hawthorne et al. (2012), whereas it is classified as edenite by Leake et al. (1997); hereafter, it is referred to as pargasite. Coarse-grained pargasite (~ 1 mm in diameter) is surrounded by, or occurs interstitial to, orthopyroxene (Fig. 3a-c). In contrast, numerous fine-grained (< 0.5 mm) and anhedral pargasite grains are widely observed as inclusions in serpentine and olivine (Fig. 3d). Fine-grained fragmental remnants of pargasite (< 100 μm) are also observed as green spots (Fig. 3d-f). The altered domains of pargasite in the green spots have chlorite-like compositions (Fig. 3f). Tremolite forms locally at pargasite rims (Fig. 3g). Spinel in the amphibole-bearing harzburgites is characteristically anhedral with "worm holes" (Fig. 4a-c) and locally associated with amphibole (Fig. 4d). Mineral inclusions and their relics are frequently observed in spinel crystals. Amphibole (magnesio-hornblende) and Na-mica (aspidorite or Na-phlogopite) form the spinel-hosted silicate mineral inclusions (Fig. 4e-f).

Major- and trace-element compositions of the minerals in the peridotites were determined using an electron microprobe analyzer (JXA-8800) at Kanazawa University and University of Tokyo, Japan (Akizawa et al., 2021). Trace-element compositions of orthopyroxene and amphibole were determined by a laser ablation-inductively coupled plasma-mass spectrometry (LA-ICP-MS) (Microlas Geolas Q-plus193/New Wave Research UP-213 laser system and Agilent 7500s ICP-MS) at Kanazawa University (Morishita et al., 2005; Tamura et al., 2022). Analyses employed a 100 μm laser beam diameter, a 6 or 10 Hz laser repetition rate, and an 8 J cm^{-2} laser energy density. A 15 μm laser beam diameter and 5 Hz laser repetition rate were used for the spinel-hosted amphibole inclusions. Element contents were calibrated using NIST 612 and the reference values from the GeoReM database (Jochum and Nohl, 2008). ^{29}Si was used as an internal standard (Longerich et al., 1996). NIST 614 and BCR-2G were used to assess the data quality in each analytical session. The major- and trace-element compositions of the minerals are listed in Tables 1-3.

The mineral compositions of the amphibole-bearing harzburgite are indistinguishable from the amphibole-free harzburgite samples. Spinel Cr# of the amphibole-bearing harzburgite is 0.8 and is as high as 0.72-0.91 in the amphibole-free harzburgite and dunite samples. Ferric Fe and TiO_2 contents of spinel are low in the harzburgites [$YFe^{3+} = Fe^{3+}/(Cr + Al + Fe^{3+}) < 0.03$; $TiO_2 < 0.01$ wt.%], and those of spinel are slightly variable in the dunite ($YFe^{3+} = 0.02$-0.05; $TiO_2 = 0.06$-0.35 wt.%) (Figs. 5-6). The contents of Fo and NiO in the olivine are dominantly 92-93 and 0.25-0.40 wt.%, respectively (Fig. 6). In the harzburgites, Mg# [Mg/(Mg + Fe)] and contents of Al_2O_3 of the orthopyroxene are 0.93 and < 0.7 wt.%, respectively. The rare earth element (REE) contents of orthopyroxene are below detection limits. Other incompatible trace elements are also considerably depleted (Ti = 1-10 μg/g; Zr = 0.01-0.1 μg/g; Y = 0.003-0.01 μg/g) (Fig. 7). For orthopyroxene, the quantitative Ti, Zr, and Y data are useful for discussing the melting process (Nishio et al., 2023).

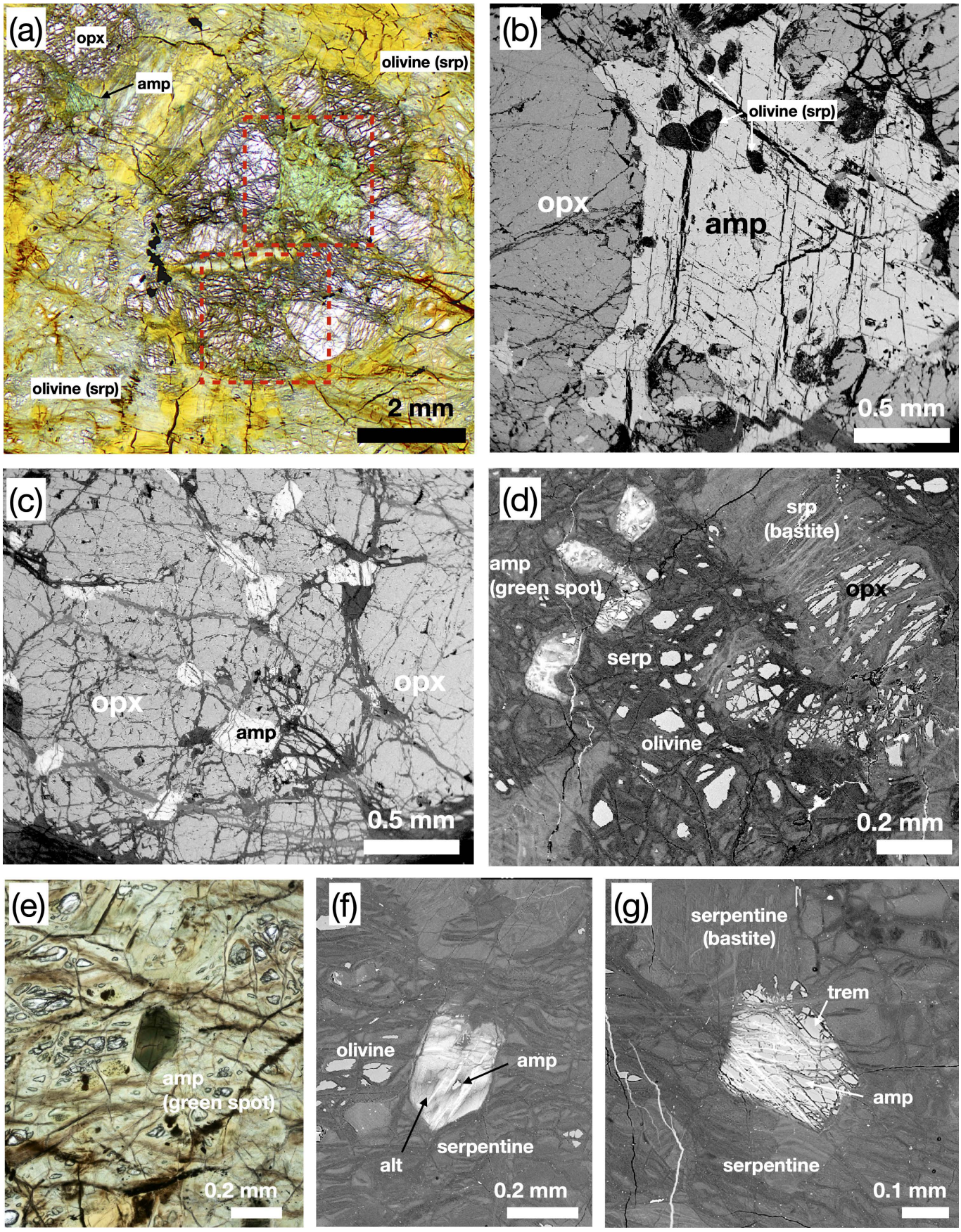

Fig. 3 - Mode of occurrence of amphibole in harzburgite (#91502) from the Horokanai complex. The amphibole (amp) is pargasitic in composition (see the text). (a-d) Green amphibole closely associated with and surrounded by orthopyroxene (opx). Note that the pargasite contains small olivine grains (serpentine). (d) Anhedral amphibole and orthopyroxene partly replaced by bastite in olivine and serpentine. Note that the amphibole is altered and fragmented. (e-f) Example of green spots distributed pervasively in the harzburgite. Fragments of amphibole remnants coexist with the altered domains (alt) that are the green spots. The altered domain is a chlorite-like mineral. (g) Tremolite (trem) formed at the rim of pargasite (amp). (a) and (c) are polarized light images and the other sub-figures are back-scattered electron images.

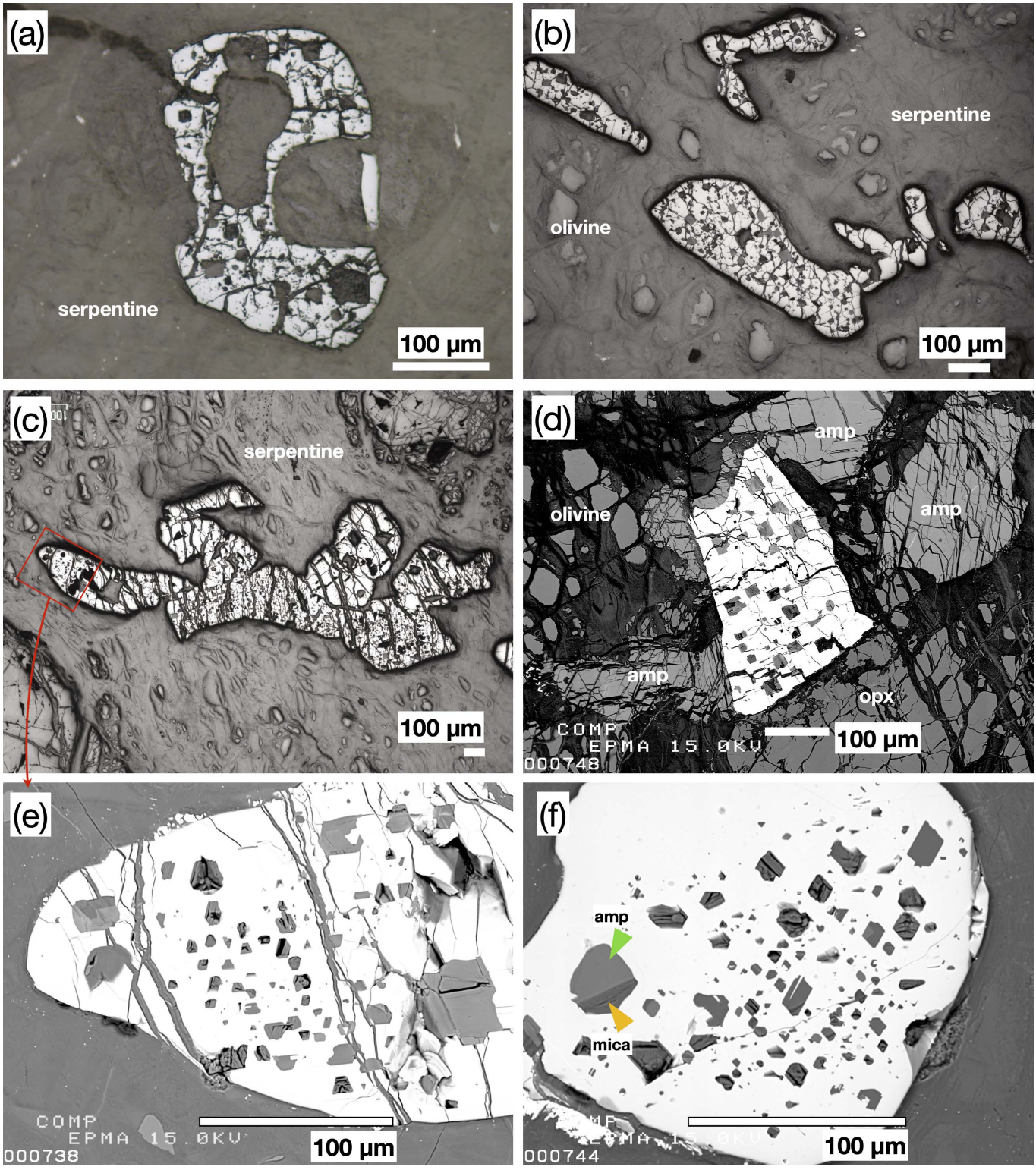

Fig. 4 - Spinel in an amphibole-bearing harzburgite (#91502) from the Horokanai complex. Note that most of the spinel is irregular in shape and contains numerous "worm holes" and inclusions. Spinel is closely associated with amphibole (amp) and orthopyroxene (opx) in (d). (e) Enlarged view of the red square in (c). Amphibole and mica (Na-phlogopite) inclusions occur in spinel in (e) and (f), and most worm holes and inclusions are altered. (a-c) = reflected light image; (d-f) = back-scattered electron image.

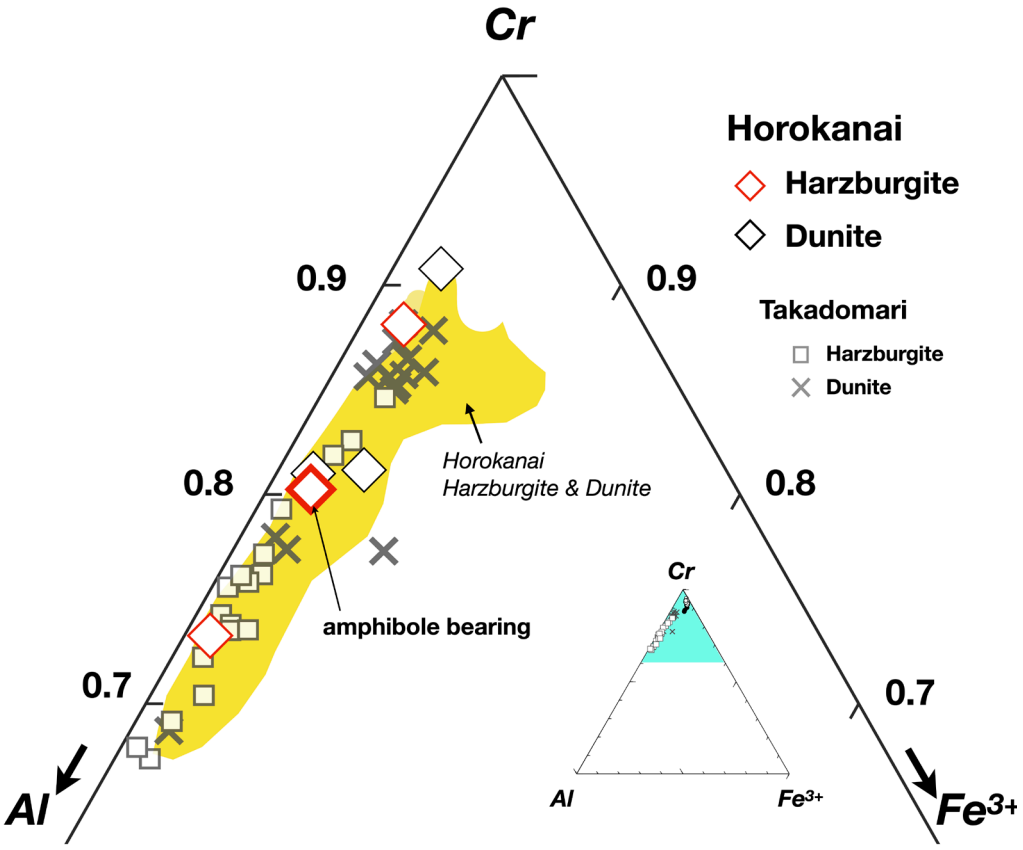

Fig. 5 - Trivalent cation diagram for spinel in harzburgite and dunite from the Horokanai complex. The Horokanai field and Takadomari data are from Ishizuka (1985), Tamura et al. (1999), and Nishio et al. (2023).

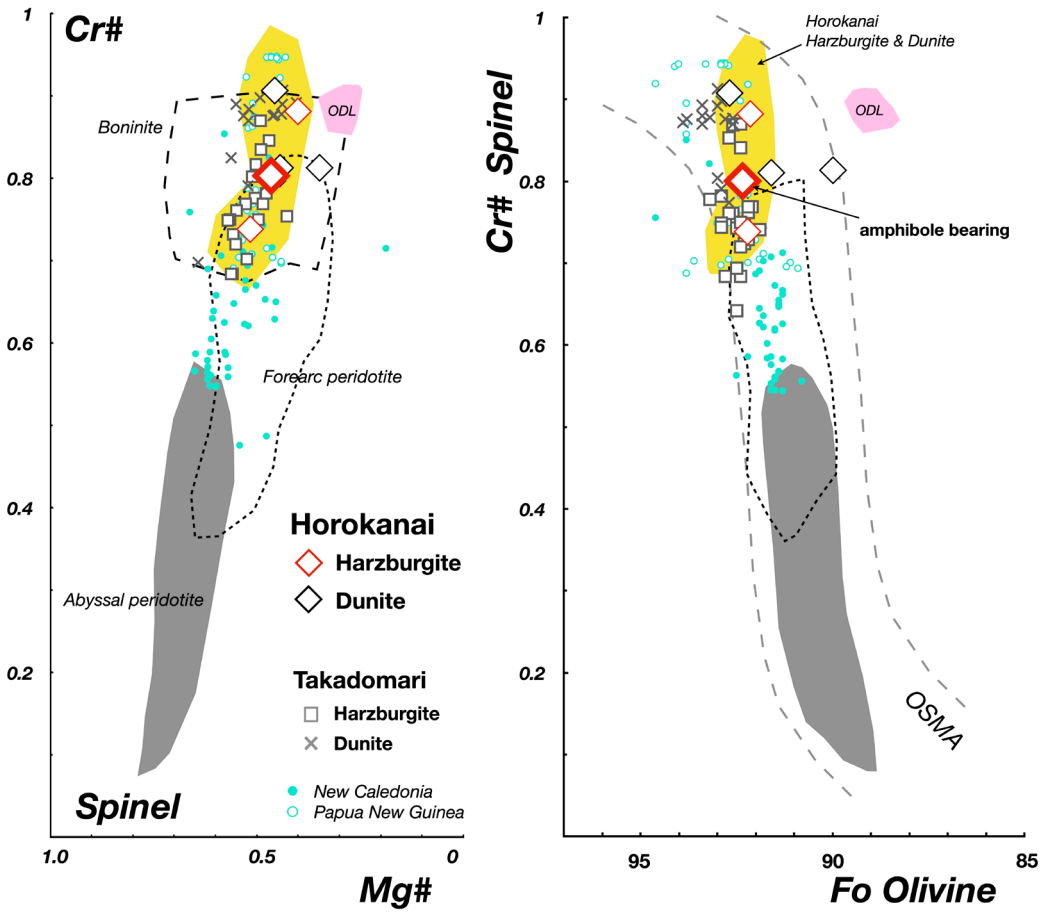

Fig. 6 - Spinel and olivine compositions in harzburgite and dunite from the Horokanai complex. (a) Spinel Mg#-Cr# and (b) olivine Fo-spinel Cr#. The olivine-spinel mantle array (OSMA) is from Arai (1987; 1994). The Horokanai field and Takadomari data are from Ishizuka (1985), Tamura et al. (1999), and Nishio et al. (2023). The compositional field of the orthopyroxenite-dunite layer (ODL) from the Horokanai ophiolite is from Iwata and Arai (unpublished data). New Caledonia and Papua New Guinea data are from Secchiari et al. (2020), Xu et al. (2021), and Barrett et al. (2022). Compositional fields for abyssal and forearc peridotites and boninites are from Tamura et al. (2006).

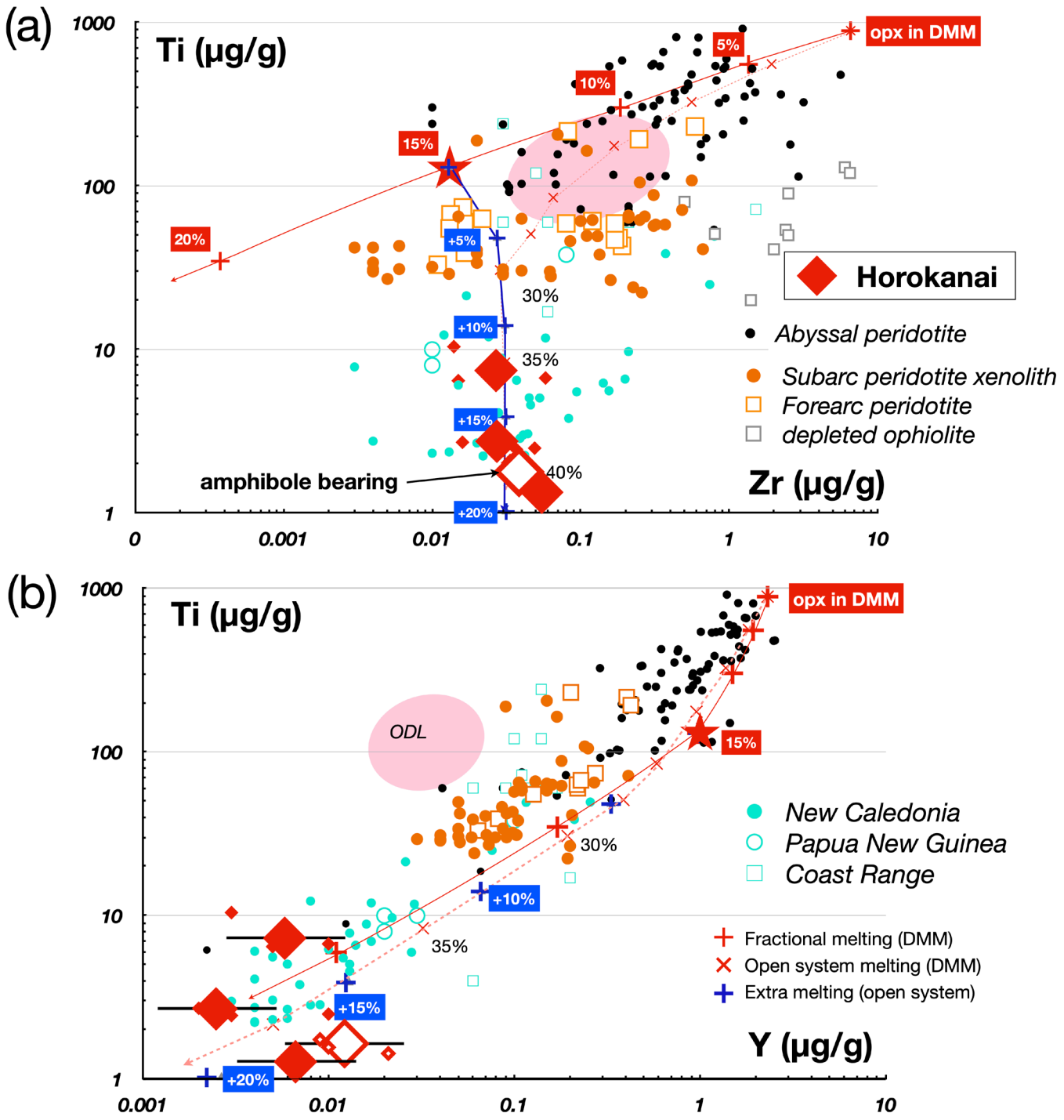

Fig. 7 - Trace-element compositions of orthopyroxene in harzburgite from the Horokanai complex. (a) Ti versus Zr. (b) Ti versus Y. Arrows and numbers indicate the melting trend and degree of melting: Red + = fractional melting of DMM; × = open-system melting of DMM; Blue + = influx melting of the residue by 15% fractional melting of DMM (star). The modeling details have been described by Nishio et al. (2023). The pink field is orthopyroxene from the orthopyroxenite-dunite layer in the Horokanai complex (Iwata and Arai, unpublished data). New Caledonia, Papua New Guinea, and Coast Range data are from Jean and Shervais (2017), Secchiari et al. (2020), Xu et al. (2021), and Barrett et al. (2022). Other data source are, for abyssal peridotites: Hellebrand et al. (2005), Tamura et al. (2008), Seyler et al. (2011), D'Errico et al. (2016), and Seyler and Brunelli (2018); for sub-arc peridotite xenoliths: Grégoire et al. (2001), Ishimaru et al. (2007), and Ionov et al. (2010); for forearc peridotites: Parkinson et al. (1992) and Birner et al. (2017); for depleted ophiolite: Bizimis et al. (2000).

Amphibole in the harzburgite is mainly pargasite (Fig. 8a). The classification of Hawthorne et al. (2012) is preferable for amphiboles in peridotite because the Cr_2O_3 content is also used. The amphibole in the Horokanai harzburgites has a distinctive composition among those reported for amphiboles in peridotites. The Mg# of the pargasite are 0.93-0.94, and the Na_2O content is 2.5 wt.%. Contents of Al_2O_3 and Cr_2O_3 are 7.6-8.7 and 2.5–2.8 wt.%, respectively (Fig. 8b). Contents of TiO_2 are very low (Ti = 130-330 μg/g). Chondrite-normalized REE and primitive mantle-normalized multi-element patterns of pargasite are shown in Fig. 9. The REE pattern of the pargasite is flat or convex-upward in shape (Fig. 9a).

Table 1 - Representative major element compositions of minerals in harzburgites and dunites from the Horokanai complex.

	Amphibole-bearing Harzburgite #91502			Harzburgite #91501			Harzburgite d1harz			Dunite Spd		Dunite mid		Dunite dunII		
	Spinel	Olivine	Opx	Spinel	Olivine	Opx	Spinel	Olivine	Opx	Spinel	Olivine	Spinel	Olivine	Spinel	Olivine	Opx
SiO_2		40.70	57.46		41.44	57.83		40.54	57.09		40.79		40.92		40.45	57.51
TiO_2								0.01		0.06	0.01	0.27	0.01	0.34		0.03
Al_2O_3	9.62		0.73	13.15		0.72	5.47		0.2	4.61		9.43		8.64		0.35
Cr_2O_3	58.40		0.39	57.30		0.28	62.44	0.01	0.16	65.35		59.36		56.01		0.17
FeO*	21.90	7.49	5.32	17.66	7.53	4.93	23.10	7.58	5.01	21.07	7.1	21.28	8.17	26.58	9.73	6.27
MnO	0.35	0.11	0.13	0.30	0.12	0.12	0.41	0.11	0.12	0.38	0.1	0.39	0.12	0.48	0.2	0.18
MgO	8.55	51.28	36.52	11.37	51.06	35.77	7.71	51.23	35.83	9.20	51.24	8.96	51.03	6.81	49.74	35.13
CaO		0.01	0.32			0.69		0.01	0.43		0.01		0.01			0.6
Na_2O			0.03					0.01	0.02		0.02		0.01			
K_2O									0.01		0.01		9			
NiO		0.40	0.08	0.03	0.39	0.05	0.04	0.37	0.06	0.03	0.31	0.02	0.25	0.04	0.36	
Total	98.82	99.99	100.95	99.82	100.53	100.40	99.17	99.85	98.93	100.70	99.58	99.71	100.52	98.90	100.55	100.33
Mg#	0.432	0.924	0.925	0.550	0.924	0.928	0.398	0.923	0.93	0.464	0.928	0.446	0.918	0.347	0.901	0.91
Cr#	0.803			0.745			0.884			0.905		0.809		0.813		
YFe^{3+}	0.026			0.014			0.033			0.031		0.020		0.055		

Mg# = Mg/(Mg + Fe^{2+}), Cr# = Cr/(Cr + Al), YFe = Fe^{3+}/(Cr + Al + Fe^{3+}); total Fe as Fe^{2+} for olivine and pyroxene. Spinel Fe^{2+} and Fe^{3+} were calculated based on stoichiometry.

Table 2 - Major-element compositions of amphibole, mica, and alteration minerals in harzburgite sample (#91502).

	Amphibole Chromio-pargasite*												
	Amp1	Amp2	Amp3		Amp4	Amp5	Amp6	Amp7	Amp8	in GS Amp9	in GS Amp10	in GS Amp11	Amp12
spot#	8	9	20	21	x41	x39	x23	x27	x24	130	148	150	(core)
SiO_2	49.14	48.64	48.53	49.14	49.77	49.19	48.90	49.80	50.09	47.27	49.24	48.37	47.99
TiO_2	0.04	0.01	0.02	0.01	0.02	0.08			0.07	0.01			0.01
Al_2O_3	8.55	8.35	8.65	8.26	8.32	8.32	8.33	8.00	8.28	8.24	7.28	7.96	8.50
Cr_2O_3	2.68	2.63	2.58	2.85	2.36	2.35	2.42	2.84	2.31	2.77	2.32	2.50	2.63
FeO*	2.45	2.34	2.79	2.23	2.28	2.40	2.52	2.66	2.37	2.77	2.35	2.49	2.67
MnO	0.08	0.06	0.09	0.04	0.07	0.08	0.07	0.05	0.08	0.06	0.05	0.06	0.06
MgO	21.19	21.13	21.35	20.84	19.73	19.65	19.82	20.14	20.45	21.70	21.07	21.37	21.09
CaO	11.09	11.68	11.23	11.97	12.43	11.97	11.68	11.72	12.04	11.35	11.94	11.65	11.33
Na_2O	2.50	2.52	2.39	2.32	2.25	2.52	2.68	2.47	2.43	2.74	2.44	2.52	2.63
K_2O	0.11	0.10	0.10	0.09	0.07	0.09	0.09	0.07	0.10	0.11	0.08	0.09	0.10
NiO	0.11	0.08	0.11	0.12	0.10	0.12	0.09	0.10	0.10	0.10	0.10	0.08	0.12
Total	97.92	97.53	97.84	97.87	97.40	96.75	96.59	97.83	98.30	97.11	96.88	97.10	97.13
Mg#	0.939	0.942	0.932	0.943	0.939	0.936	0.933	0.931	0.939	0.933	0.941	0.939	0.934

	Amphibole (spinel inclusion) Magnesio-hornblende*				Na-mica (spinel inclusion) aspidolite				Alterd domain in GS with amp	with amp		Serpentine serpentine	bastite
	SPINX1	SPINX2	SPINX3	SPINX4	SPINX5	SPINX6	SPINX7	SPINX8					
spot#	x2	x6	x11	X27	x4	x5	x9	x10	128	151	15	145	153
SiO_2	50.57	50.71	52.52	49.80	43.61	43.49	42.54	43.02	34.17	36.97	36.76	39.04	38.81
TiO_2	0.08		0.02		0.04	0.10	0.06	0.07	0.01	0.02			
Al_2O_3	7.05	5.11	5.93	8.00	14.15	13.35	14.18	14.28	5.17	2.23	1.83	0.10	0.37
Cr_2O_3	2.40	3.06	2.73	2.84	2.88	3.23	2.93	2.85	2.69	2.07	2.16	0.03	0.26
FeO*	2.25	2.02	2.09	2.66	1.17	1.26	1.26	1.35	16.95	9.29	8.57	4.65	8.13
MnO	0.06	0.09	0.09	0.05		0.01		0.02	0.28	0.10	0.12	0.07	0.23
MgO	20.62	20.71	21.64	20.14	25.84	25.45	25.06	25.16	27.68	33.91	35.39	39.91	34.75
CaO	12.11	10.63	11.29	11.72	0.01			0.01	0.03	0.07	0.04	0.05	0.16
Na_2O	2.05	2.08	2.23	2.47	5.55	5.46	5.36	5.43		0.02		0.02	0.02
K_2O	0.10	0.11	0.07	0.07	0.50	0.44	0.63	0.44		0.00			0.01
NiO	0.09	0.09	0.07	0.10	0.26	0.21	0.24	0.23	0.10	0.08	0.11	0.35	0.02
Total	97.38	94.61	98.67	97.16	94.00	92.99	92.27	92.84	87.08	84.76	84.98	84.21	82.77
Mg#	0.942	0.948	0.949	0.945	0.975	0.973	0.973	0.971	0.744	0.867	0.880	0.939	0.884

* nomenclature of amphibole from Hawthorne et al. (2012); GS: green spot with/without amphibole remnant.

Table 3 - Trace-element compositions of orthopyroxene, amphibole, and alteration minerals in harzburgite sample (#91502).

	Orthopyroxene					Amphibole											Spinel-	Greenspot	Serpentine		Reference material				
	#91502	#91501	#91501-2	d1harz		Amp1		Amp2		Amp3		Amp4	Amp5	Amp6	Amp7	inclusion	ALT		DL	NIST614		BCR2G		
spot#	LA101	LA103	LA201	LAd01	Opx2	P01	LA2_101	P02	LA2_102	P03	LA2_103	LA101	LA102	LA103	X02	SPINX1	LA102	LA103	LA100	LA1_614	R.V.	BCR	R.V.
Li	2	–	–	–	3	18	17	15	15	12	16	5	8	7	6	–	0.11	0.36	0.11	1.8	1.6	8.8	9
B	3.5	–	–	–	0.3	2	1	3	3	5	2	2	2	2	3	–	4.0	4.5	0.39	1.8	1.4	8.9	6
Sc	12	–	–	–	16	122	110	124	99	117	110	140	151	136	112	–	166	3.4	0.06	7.6	1.6	37	33
Ti	1.4	1.2	6.4	2.4	1.7	335	250	222	174	136	140	20	21	42	28	149	77	0.95	0.17	3.2	3.4	14,603	14,100
V	16	–	–	–	43	335	341	301	292	272	324	272	303	282	231	–	355	1.7	0.03	1.1	1	398	425
Cr	1,143	–	–	–	2,608	19,144	19,404	18,391	17,013	15,745	18,290	13,518	14,336	15,040	14,119	12,725	17,351	85	0.58	1.1	1.8	15	17
Co	59	–	–	–	53	32	34	31	31	30	29	26	32	30	31	–	14	108	0.04	0.8	0.85	37	38
Ni	846	–	–	–	643	875	890	849	780	776	817	589.9	657.5	629.4	615.7	–	736	1,846	0.32	1.2	1	14	13
Rb	0.14	–	–	–	0.24	0.8	0.8	0.9	0.9	2.4	2.3	1.1	1.1	1.0	1.3	–	0.05	0.03	0.02	0.9	0.86	43	47
Sr	0.14	0.012	0.066	0.089	0.11	82.3	71.1	70.3	55.7	48.7	42.9	47.5	58.0	65.0	43.3	61	0.23	0.50	0.01	44.4	45.8	343	342
Y	0.021	0.004	0.005	0.003	0.009	1.1	0.9	0.9	0.7	0.6	0.5	0.2	0.2	0.3	0.2	0.3	0.54		0.004	0.73	0.80	35	35
Zr	0.02	0.04	0.015	0.037	0.04	5.5	4.2	4.5	3.2	2.1	2.0	0.8	0.9	1.2	0.7	2.8	1.84	0.06	0.008	0.74	0.84	183	184
Nb	0.01	0.03	0.014	0.012	0.02	1.6	1.3	1.1	0.9	0.5	0.5	0.3	0.4	0.4	0.4	0.3	0.62		0.005	0.79	0.81	13	13
Ba	0.1				0.3	10.3	9.5	14.6	9.4	16.3	15.4	11.0	13.3	14.3	10.6	12.3	0.07	0.18	0.02	3.08	3.2	679	683
La						0.204	0.162	0.118	0.081	0.063	0.050	0.053	0.070	0.067	0.050		0.09		0.002	0.71	0.72	27.04	24.7
Ce						0.807	0.680	0.452	0.328	0.195	0.185	0.155	0.203	0.205	0.141	0.16	0.311	0.009	0.002	0.81	0.81	53.39	53.3
Pr						0.151	0.125	0.095	0.061	0.035	0.031	0.026	0.033	0.035	0.023	–	0.044		0.002	0.76	0.76	7.14	6.7
Nd						0.897	0.726	0.605	0.396	0.195	0.172	0.146	0.173	0.184	0.120		0.230		0.011	0.73	0.74	30.51	28.9
Sm						0.294	0.229	0.212	0.138	0.075	0.059	0.036	0.043	0.053	0.034		0.078		0.016	0.72	0.75	6.91	6.59
Eu						0.074	0.057	0.052	0.033	0.025	0.025	0.019	0.024	0.023	0.017		0.024		0.004	0.72	0.76	2.07	1.97
Gd						0.318	0.249	0.223	0.177	0.087	0.078	0.041	0.060	0.067	0.037		0.095		0.018	0.73	0.75	7.01	6.71
Tb						0.045	0.036	0.032	0.023	0.016	0.015	0.006	0.007	0.011	0.011	–	0.017		0.003	0.68	0.73	1.06	1.02
Dy						0.272	0.210	0.194	0.147	0.107	0.093	0.048	0.056	0.060	0.052		0.103		0.008	0.72	0.74	6.91	6.44
Ho						0.043	0.037	0.036	0.026	0.024	0.020	0.009	0.009	0.011	0.008	–	0.019		0.004	0.72	0.74	1.35	1.27
Er						0.108	0.086	0.077	0.062	0.061	0.057	0.026	0.026	0.035	0.024		0.059		0.008	0.69	0.74	3.83	3.70
Tm						0.014	0.012	0.013	0.009	0.010	0.010	0.005	0.006	0.007	0.004	–	0.008		0.004	0.70	0.73	0.56	0.51
Yb						0.09	0.08	0.10	0.07	0.09	0.09	0.077	0.071	0.074	0.059		0.075		0.01	0.73	0.77	3.77	3.39
Lu						0.02	0.02	0.02	0.01	0.02	0.02	0.019	0.018	0.020	0.015		0.019		0.004	0.70	0.73	0.56	0.50
Hf						0.17	0.15	0.16	0.12	0.06	0.07	0.007	0.014	0.019	0.021	–	0.032		0.016	0.66	0.7	4.97	4.84
Ta						0.06	0.05	0.05	0.04	0.02	0.02	0.00	0.01	0.01	0.01	–	0.021		0.005	0.78	0.79	0.9	0.78
Pb						0.38	0.49	0.33	0.30	0.12	0.11	0.44	0.53	0.57	0.48		0.054		0.026	2.49	2.320	10.2	11.00
Th																			0.005	0.70	0.748	6.5	5.90
U																			0.004	0.91	0.823	1.6	1.69

DL: detection limit. R.V.: reference value (GeoReM database : Jochum and Nohl, 2008); Blank: data below the detection limit. – : not analyzed.

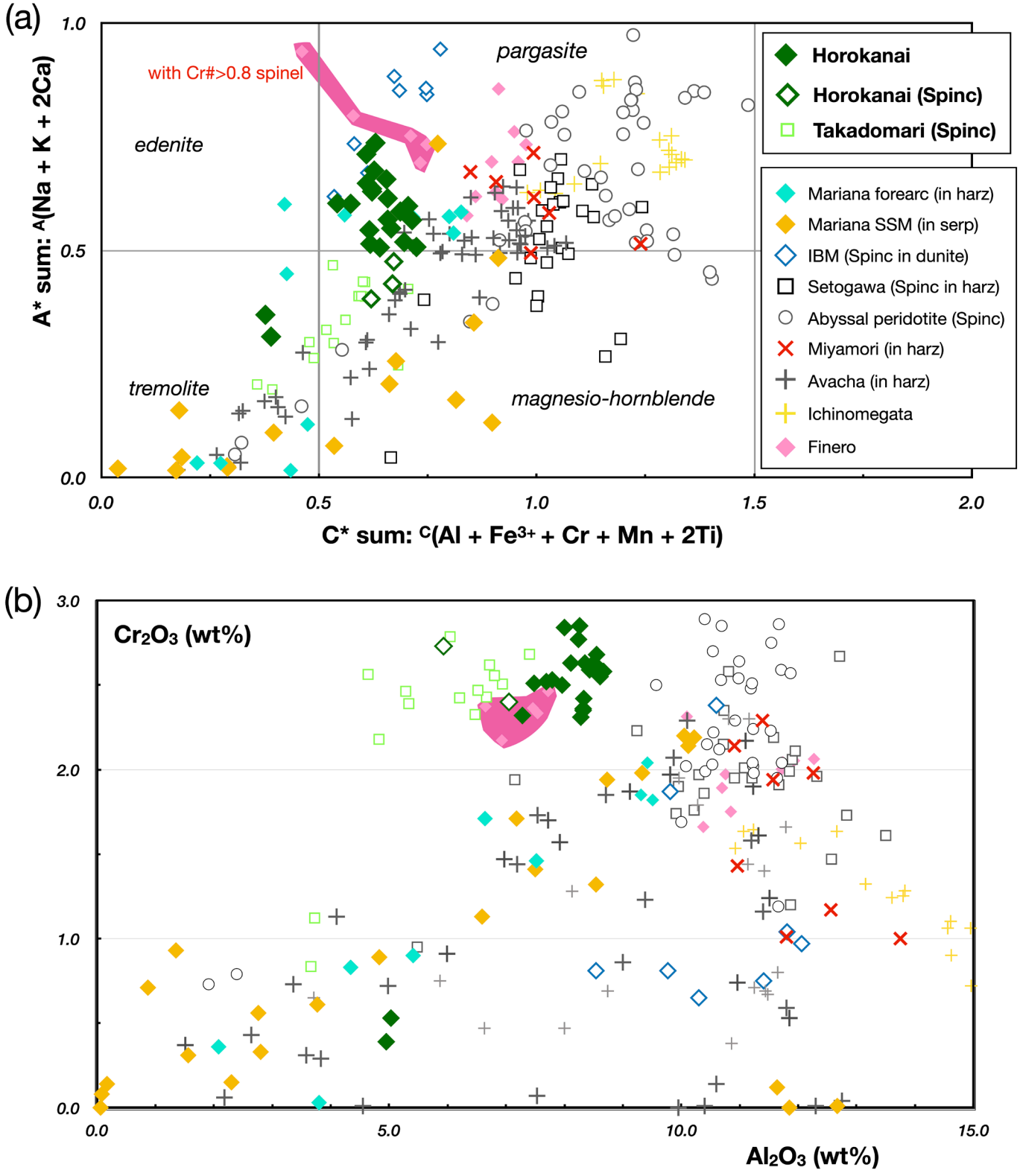

Fig. 8 - Composition of amphibole in harzburgite from the Horokanai complex. (a) Amphibole classification based on Hawthorne et al. (2012). The diagram and data calculations were obtained using the spreadsheet of Locock (2014). (b) Plot of Cr_2O_3 versus Al_2O_3. Reference data: for Mariana forearc: Ohara and Ishii (1998) and Chen and Zeng (2007); for Mariana serpentine seamount: Ishii et al. (1992), Parkinson and Pearce (1998), and Ichiyama et al. (2021); for Miyamori ophiolite: Ozawa (1988); for sub-arc mantle xenoliths: Ishimaru et al. (2007), Ionov (2010), and Bénard amd Ionov (2013); for spinel-hosted amphibole inclusions (Spinc) in abyssal peridotite and troctolite: Tamura et al. (2014; 2016); for Setogawa harzburgite: Arai et al. (2022); for Izu-Bonin-Mariana arc harzburgite: Morishita et al. (2011); for Finero peridotite: Zanetti et al. (1999). Finero amphiboles coexisting with high-Cr# spinel (> 0.8) are highlighted (see the text).

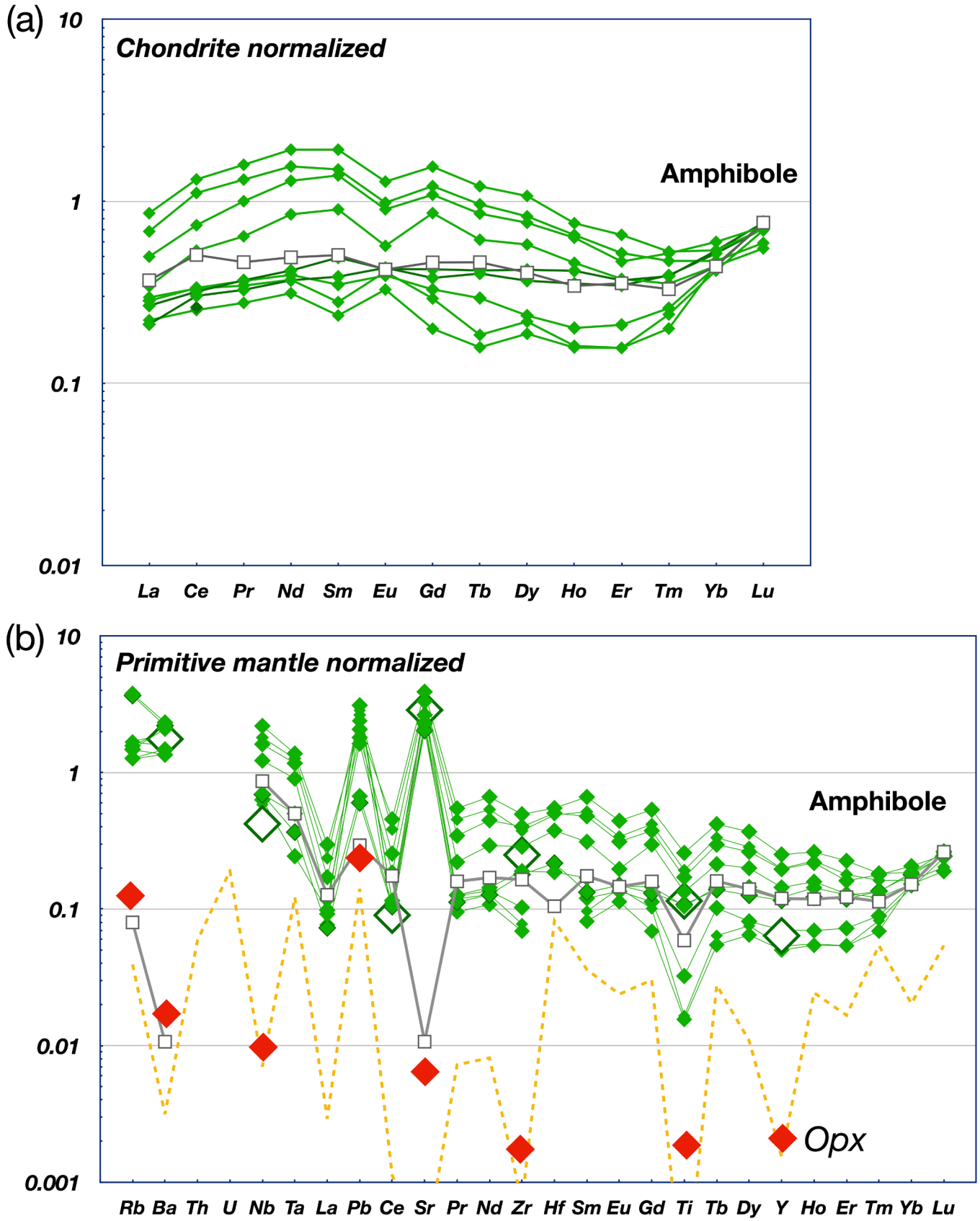

Fig. 9 - Trace-element compositions of amphibole in harzburgite from the Horokanai complex. (a) Chondrite-normalized REE patterns. (b) Primitive mantle-normalized trace-element patterns. Open green diamonds indicate spinel-hosted amphibole inclusions. Open square pattern indicates chlorite-like domain in green spot (e.g., Fig. 3f). An orthopyroxene composition (red diamond) with the detection limit of the analyses (broken line) is shown for comparison in (b). Normalization values are from Sun and McDonough (1989). Normalization values are from Sun and McDonough (1989). The reader is referred to the PDF online for a colour version.

Both patterns exhibit a gentle downward slope from Sm to La and from Lu to Er. The convex-upward patterns exhibit higher abundances of REEs with a small negative Eu anomaly. In a multi-element diagram (Fig. 9b), Nb and Ta are markedly enriched relative to light REEs (LREEs), whereas Ti is weakly depleted relative to neighbouring REEs. Strontium and Pb are relatively enriched, whereas Th and U are depleted and below detection limits. These features result in high Ba/Th ratios (> 2000) and large positive Sr and Pb anomalies in the trace-element patterns (Fig. 9b). Spinel-hosted amphibole inclusions have similar major-element compositions to the pargasite, although some amphibole data can be classified as magnesio-hornblende (Fig. 8a). The trace-element abundances of Ti, Sr, Zr, Nb, Ba, Ce, and Y in the amphibole inclusions are similar to those of pargasite (Fig. 9). Inclusions of mica in the spinel are aspidorite (Na-phlogopite). Contents of Na_2O and K_2O are 5.4 and 0.5 wt.%, respectively. Contents of Cr_2O_3 are 2.8-3.2 wt.%.

Altered domains in the green spots have chlorite-like compositions, with higher Cr_2O_3 (1.8-2.8 wt.%) and Al_2O_3 (1.8-7.3 wt.%) than serpentine and bastite (<< -0.4 wt.%) (Table 2). Contents of CaO and Na_2O are very low (<< -0.1 wt.%) in altered domains relative to coexisting pargasite. The REE patterns of the altered domains are flat and similar to those of pargasite (Fig. 9a). Ratios of Nb/La and Ta/La are as high as those of pargasite, and Sr is highly depleted (Fig. 9b).

DISCUSSION

Origin of the Horokanai peridotite

Magnesian olivine (Fo = 91-93) and orthopyroxene (Mg# = 0.93) in the studied harzburgites and dunites from the Horokanai complex are typical of mantle-derived peridotites (e.g., Fig. 6a). The Cr# of spinel and incompatible element abundances of clinopyroxene are good indicators of the degree of melting of mantle-derived residual peridotites (e.g., Arai, 1987; 1994a; Hellebrand et al., 2001). The Cr# of spinel in the studied peridotites is extremely high (Cr# > 0.7) compared with those of spinel in abyssal peridotites (Figs. 5-6). The clinopyroxene-free modal composition of the harzburgites is consistent with the spinel compositions, indicating a very high degree of melting.

We now evaluate the abundances of incompatible elements in orthopyroxene. The Ti and Y abundances of orthopyroxene are considerably depleted compared with orthopyroxene in harzburgites from forearc regions and subarc mantle xenoliths (Fig. 7b). Similar orthopyroxene compositions have been reported for ultra-depleted peridotites in Papua New Guinea and New Caledonia ophiolites (Secchiari et al., 2020; Xu et al., 2021; Barrett et al., 2022). These modal compositions and the mineral chemistry suggest that the harzburgites from the Horokanai complex are residues after very high degrees of melting. In contrast to the extreme depletion of Ti and Y in orthopyroxene in the Horokanai harzburgites, Zr contents are as high as those of orthopyroxene in highly depleted peridotites and depleted abyssal peridotites produced by 15% fractional melting of Depleted MORB Mantle (DMM, Fig. 7a). Nishio et al. (2023) demonstrated that the Ti-Zr-Y abundances of orthopyroxene in ultra-depleted harzburgites can be reproduced by the open-system melting model of Ozawa (2001). Although fractional melting of the DMM cannot reproduce the Ti-Zr-Y compositional variations, influx melting with a subducted slab-derived fluid-melt can reproduce these at very high degrees of melting (F = 35%-45%; Fig. 7). Similar to the remelting process proposed for boninite formation (e.g., Umino et al., 2015; 2018), extensive influx melting of depleted peridotite produced by 15% fractional melting can also cause effective depletion of Ti along with enrichment of Zr (Fig. 7a). As such, slab-derived influx melting was involved in the formation of the Horokanai harzburgites.

Based on experimental data and phase diagrams, H_2O enhances the degree of melting of peridotite by lowering the liquidus temperature, and hydrous conditions also cause incongruent melting, in which SiO_2-rich melt is produced by the dissolution of orthopyroxene and precipitation of olivine (Kushiro, 1972). The anhedral and fine-grained orthopyroxene (Fig. 2) and its low modal abundance (5-15 vol.%) in the studied peridotites may have resulted from incongruent melting after clinopyroxene was completely consumed. The influx melting discussed above is not inconsistent with melting under hydrous conditions.

Origin of amphibole - from trapped melt?

Amphiboles such as pargasite, magnesio-hornblende, or tremolite have often been identified in metasomatized peridotite xenoliths from arc settings (e.g., Grégoir et al., 2001; Ishimaru and Arai, 2008; Ionov, 2010). They are also found in peridotites from the ocean floor (Fig. 8) (e.g., Ishii et al., 1992; Ohara and Ishii, 1998; Parkinson and Pearce, 1998; Ichiyama et al., 2021). Amphiboles in the xenoliths are thought to be the products of hydrous metasomatism in the mantle wedge, whereas amphiboles in the ocean floor peridotites have been explained by metamorphism/metasomatism by hydrous fluids in the post-melting stage. However, an origin as a residual phase or by crystallization from a trapped hydrous melt cannot be excluded (e.g., Ozawa, 1988; Parkinson and Pearce, 1998).

Coarse-grained pargasite is associated with orthopyroxene, but it is interstitial to orthopyroxene in the studied harzburgite (Fig. 3a-c). The green spots pervasively distributed in the harzburgite indicate that the pargasite was also formed interstitial to olivine (Fig. 3d-f). Amphibole is associated with Na-mica as spinel-hosted inclusions, although most of this amphibole is altered (Fig. 4). Based on these occurrences, we propose that amphibole crystallized from melt trapped during the melting stage, which formed the ultra-depleted peridotites.

Major-element compositions of the amphibole are similar for the coarse grains, fragments in the green spots, and spinel-hosted inclusions. The pargasite has a distinctive composition (e.g., high Cr_2O_3 content) compared with those reported for amphiboles in peridotites (Fig. 8). Similar pargasites have been reported in phlogopite peridotites from the Finero complex, Italy (Zanetti et al., 1999). The Finero amphiboles are not only Cr_2O_3-rich (2.5 wt.%) (Fig. 7b), they also coexist with very high-Cr# spinel (> 0.8). Given the enrichment of incompatible elements (Fig. 10), the amphibole in the Finero peridotites has been interpreted as having been formed by the reaction between slab-derived melts and peridotite and subsequent metasomatism (Zanetti et al., 1999). However, the studied pargasite is not enriched in incompatible elements (Fig. 10). As such, the geochemical features of pargasite in the Horokanai harzburgite probably represents a partial melt rather than a slab-derived melt.

Spinel-hosted hydrous silicate mineral inclusions have been widely reported in peridotites (e.g., Tamura et al., 2014). Their origin remains controversial but may represent

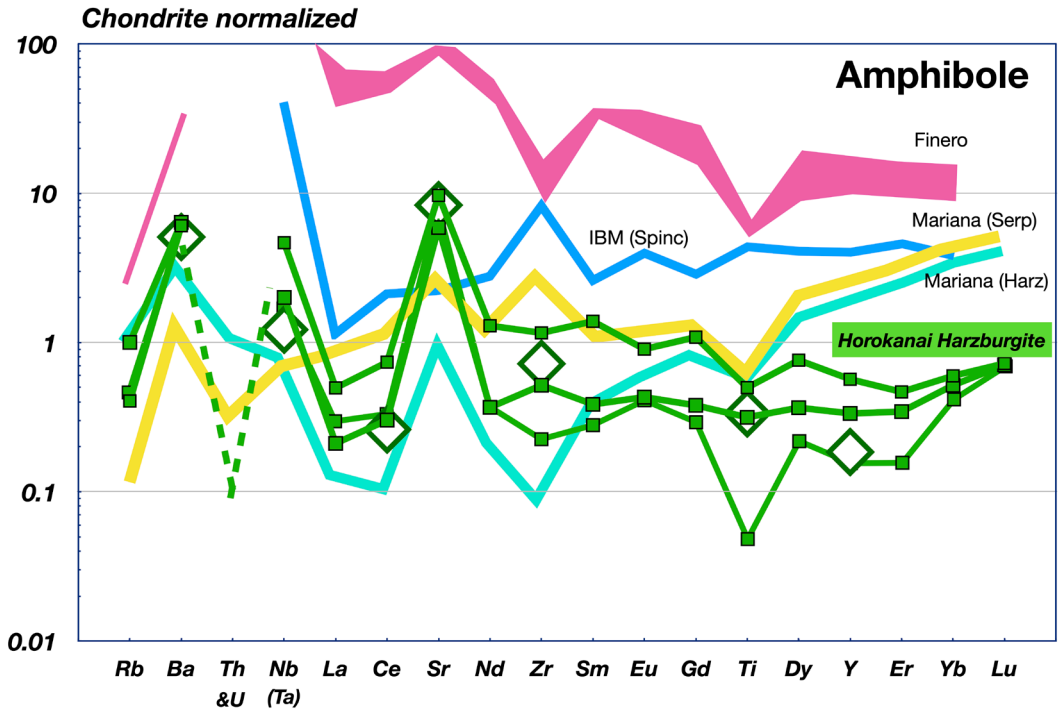

Fig. 10 - Comparison of the trace-element compositions of amphiboles between harzburgite from the Horokanai complex and other peridotites. The three representative patterns (enriched, flat and concave REE patterns: Fig. 9a) and the inclusion composition (open diamond) of amphiboles are shown. Broken line indicates a negative anomaly of Th (and U) estimated from the detection limit. For Mariana forearc: harzburgite from Chen and Zeng (2007) and serpentinite from Ichiyama et al. (2021); for IBM spinel inclusion in harzburgite: Morishita et al. (2011); for Finero peridotite: Zanetti et al. (1999). Normalization values are from Sun and McDonough (1989).

the reaction products in replacement dunites or during the formation of chromitite (e.g., Arai et al., 1997). SiO_2-rich melt generated instantaneously by incongruent melting of orthopyroxene during the reaction between peridotite and melt is important in the formation of the inclusions. Differentiation of the instantaneous SiO_2-rich melt is critical for the crystallization of hydrous silicate minerals in spinel (Arai et al., 1997; 2022). High-degree melting of harzburgite under hydrous conditions also generates SiO_2-rich melt by incongruent melting of orthopyroxene (Kushiro, 1972). In addition to spinel with hydrous silicate inclusions in the amphibole-bearing harzburgite, anhedral spinel with worm holes indicates that spinel was involved in the melting process (Fig. 4). Given that spinel is Cr-rich, the trapped SiO_2-rich melt can exist in the residual harzburgite and finally crystallize amphibole. Previous studies have described Cr-rich spinel (Cr# > 0.6) developed between hydrous silicate mineral inclusions and Al-rich host spinel (Cr# ~ 0.5) (Borisova et al., 2012; Arai et al., 2022). This indicates that the SiO_2-rich melt crystallizing the hydrous minerals was in equilibrium with Cr-rich rather than Al-rich spinel.

Olivine relics in coarse-grained pargasite in the harzburgite (e.g., Fig. 3a-b) support the scenario that the pargasite formed from SiO_2-rich melt after olivine precipitation during the incongruent melting of orthopyroxene. The melting occurred under hydrous conditions and, therefore, the melt was saturated in amphibole. Variations in the trace-element compositions of the pargasite, such as the high REE abundances and negative Eu anom

Linking pargasite to the boninitic melt in the mantle wedge

Highly depleted peridotites may be source residues of arc magmas, and the relationship with boninite magmatism in forearcs has been investigated in previous studies (e.g., Pearce et al., 1992). The Cr# of spinel in residual peridotites reflects the degree of melting and can identify the relationship to the extracted melt (Arai, 1994a, 1994b). The Cr# of spinel in boninite is > 0.7 (Fig. 6). Equivalent Cr# for spinel has been reported for dunite, pyroxenite, and chromitite in harzburgites from ophiolites, which form mainly owing to reactions between peridotite and boninitic melt (Valfarvy et al., 1996; Suhr et al., 2003; Tamura and Arai, 2006a; Xu et al., 2021). High-Cr# spinel harzburgite may also form as a reaction product rather than by high-degree melting alone. Conversely, the exceptionally depleted orthopyroxene compositions in the studied harzburgites indicate the high-Cr# spinel was caused by very high degrees of melting (Fig. 7b). This indicates that the harzburgites from the Horokanai complex represent residues that generated boninitic melts.

The lower crustal section of the Horokanai ophiolite comprises the orthopyroxenite-dunite layer, as shown in Fig. 1b (e.g., Ishizuka, 1985). Its origin is still controversial, but cumulates or melt-mantle reaction products are the most likely explanations. The high Cr# of spinel (> 0.85) in the layer indicates that a boninite-like highly depleted melt was produced (Fig. 6). However, no boninite volcanics have been reported in the ophiolitic complex. Instead, MORB-like volcanic rocks with seafloor metamorphism constitutes the upper crust section of the Horokanai ophiolite (Fig. 1b). Boninite volcanism probably occurred on the oceanic crust, as observed in the Oman ophiolite (e.g., Ishikawa et al., 2002). If this is true, the boninite sequence may have been lost due to tectonic erosion.

According to melting experiments on peridotites, low-pressure (P < 1 GPa) and/or hydrous conditions are favorable for the generation of boninitic melts, because primitive SiO_2-rich melt can be produced (Umino and Kushiro, 1989; Falloon and Danyushevski, 2000). As discussed above, the orthopyroxene compositions in the Horokanai harzburgites can be reproduced by very high degrees of melting with the involvement of slab-derived melt-fluid (Fig. 7); the pargasite formed from this trapped melt. The incompatible element composition of the pargasite in the studied harzburgites is distinct from amphibole in other peridotites, for example, very low abundance of HREE (Fig. 10). We calculated the

REE composition of melt in equilibrium with the pargasite using the distribution coefficients of Shimizu et al. (2017). The equilibrium melt is considerably depleted relative to MORBs. In terms of the U-shaped REE patterns or LREE-enriched patterns and has a similar REE pattern to high-Si boninite from Ogasawara and low-Ca boninite from Papua New Guinea and New Caledonia (Fig. 11) (König et al., 2010; Cluzel et al., 2016; Umino et al., 2015; 2018). As well as enrichment in LREEs, fractionation between heavy REEs [(Tm/Lu)N < 1] is characteristic of both the calculated melt and boninites (Fig. 11). Additionally, the high Cr content of the pargasite (Fig. 7b) indicates that the equilibrium melt was Cr-rich. This is consistent with the compositional characteristics of boninite.

Nisiho et al. (2022) demonstrated through model melting that the instantaneous melt of high-degree melting producing ultra-depleted peridotite is significantly depleted in incompatible elements (e.g., Ti and Y) compared to boninite. The authors predicted that boninites are either the accumulated melt of the partial melting or have undergone fractionation from and/or input to the primary melt prior to eruption. The calculated melt in equilibrium with the pargasite is also more depleted in some HREEs relative to boninite (Fig. 11). This probably indicates that the pargasite was derived from more primary melt trapped in ultra-depleted residue in the mantle wedge.

König et al. (2010) demonstrated that slab-derived melt is typically involved in the formation of LREE-enriched boninite and that slab-derived fluids were involved in the formation of LREE-depleted boninite (e.g., Troodos ophiolite). Cluzel et al. (2016) suggested that LREE-enriched boninite from New Caledonia was formed by influx melting of the depleted mantle that was re-enriched by slab-derived silicic melts. Li et al. (2013) proposed that low-Ca boninites from Ogaswara formed by partial melting of depleted mantle with a small contribution (3%) from slab-derived melt. Prouteou et al. (2001) suggested that the reaction between peridotite and slab-derived adakitic melts forms orthopyroxene with Na-rich amphibole and K-rich mica. Adakitic melt may have produced the hydrous minerals and driven the metasomatism in the Finero complex (Zanetti et al., 1999; Prouteou et al., 2001). In contrast, pargasite and Na-phlogopite in the Horokanai harzburgites suggest the sodic melt was generated by melting in the mantle wedge. High-Na and low-K rhyodacite has rarely been reported in ophiolitic complexes (e.g., Maulana et al., 2019; Qiao et al., 2022). Qiao et al. (2022) proposed that the rhyodacite is another candidate for the slab-derived melt, which formed by the melting of MORB-like crust beneath the forearc region at low pressures (P = 0.5-1.0 GPa). As such, we propose that a high-Na and low-K silicic melt was also suitable for the production of boninitic melt in the mantle wedge, although the relative timing between slab-derived melt involvement and melting cannot be constrained. Therefore, the Horokanai complex may be an example of a sodic ultra-depleted residue formed by trapped melt at a shallower depth in the mantle wedge. The compositions of such slab-derived melts might constrain the tectonic setting of some ultra-depleted peridotites.

CONCLUSIONS AND IMPLICATIONS

Residual peridotites from the Horokanai complex are extremely depleted, including features such as a total absence of clinopyroxene, very low abundances of incompatible elements in orthopyroxene, and high-Cr# spinel. Melting models of the orthopyroxene compositions show the harzburgites can be explained by influx melting (> 30%). In the pargasite-bearing harzburgite sample, spinel-hosted mineral inclusions probably record local reactions between trapped melt and spinel during melting. This implies that sodic ultra-depleted residue is produced during the generation of boninitic melt in a mantle wedge.

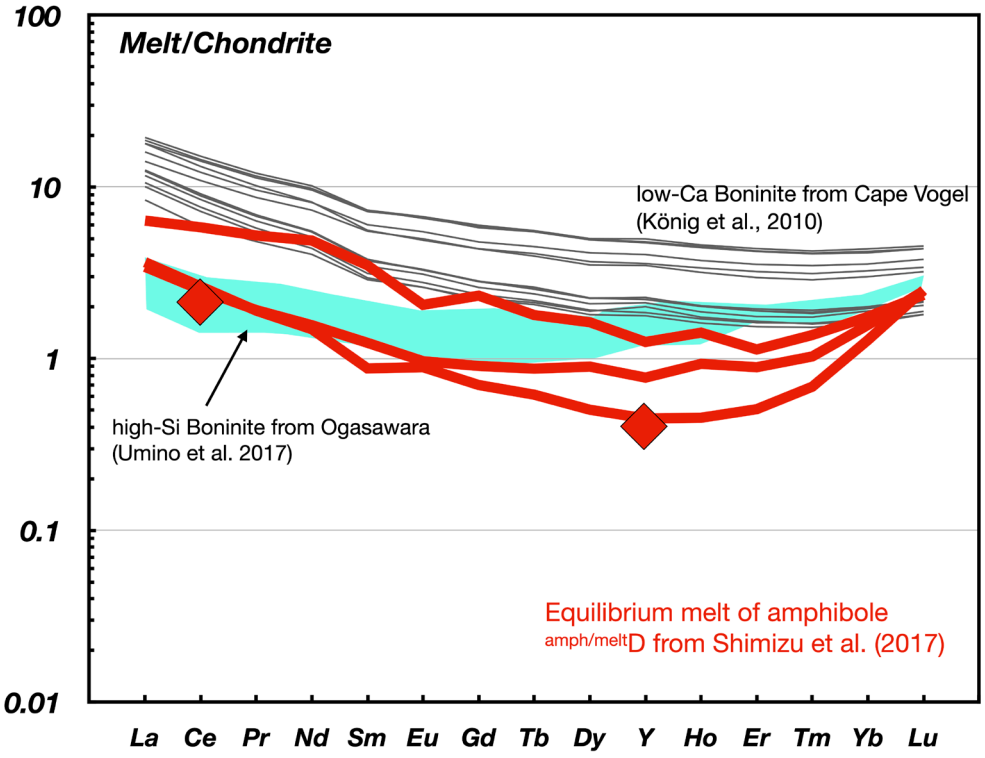

Fig. 11 - Rare earth element compositions of calculated melts in equilibrium with pargasite in the Horokanai harzburgite. The three amphibole and inclusion compositions shown in Figure 10 were used in the calculation. Amphibole/melt partition coefficients are from Shimizu et al. (2017). Boninite melt data are from König et al. (2010) and high-Si boninite data are from Umino et al. (2015; 2018).

Sodium-rich tremolite has been observed in dunite from the Horokanai complex (Ishizuka, 1980). A chromian richterite rock, which probably formed owing to metasomatism of orthopyroxenite, has also been reported (Ishii et al., 2002). In the studied amphibole-bearing harzburgite, a Cr-rich, chlorite-like phase in the green spots is probably formed by decomposition and alteration of pargasite because pargasite remnants often coexist (Fig. 3d-f). Tremolite occurs at pargasite rims (Fig. 3g). These indicate that Ca, Na, and Sr were released from the pargasite (Fig. 9b). We infer that a fluid rich in these elements was generated by the decomposition of pargasite in the harzburgite. As such, pargasite is a source of metasomatic fluid that can form sodic amphiboles during low-temperature alteration stage. Ultra-depleted peridotite represents a source of Na. The elements causing the metasomatism were possibly derived from a slab-derived melt and then preserved in the residual peridotites.

Orthopyroxenite–dunite layers occur in the Moho transition zone in the Horokanai complex, but no boninite has been observed (Fig. 1c) (e.g., Ishizuka, 1985). Although the olivine is Fe-rich (Fo ~ 89) and the orthopyroxene has high contents of incompatible elements, the spinel Cr# is as high as those of ultra-depleted peridotites from the mantle section (Figs. 6-7) (Iwata and Arai, unpublished data). Ishizuka (1985) interpreted these layers as cumulates. The involvement of boninitic melt has been proposed for the origins of orthopyroxenites in ophiolites (e.g., Varfalvy et al., 1996; Tamura et al., 2006). Further investigation of these layers will contribute to our understanding of boninitic magmatism and the crust–mantle boundary in supra-subduction zones.

ACKNOWLEDGMENTS

We thank S. Umino and T. Mizukami for discussions about this research. We also thank N. Akizawa for help with the microprobe analyses, and N. Hasebe and K. Fukushi for assistance in the laboratory. This manuscript was improved by the comments from C. Zhang and an anonymous reviewer. A. Sanfilippo, C.Z. Liu, and A. Montanini are thanked for their editorial assistance.

REFERENCES

Akizawa N., Ohara Y., Okino K., Ishizuka O., Yamashita H., Machida S., Sanfilippo A., Basch V., Snow J.E., Sen A., Hirauchi K.-I., Michibayashi K., Harigane Y., Fujii M., Asanuma H. and Hirata T., 2021. Geochemical characteristics of back-arc basin lower crust and upper mantle at final spreading stage of Shikoku Basin: an example of Mado Megamullion. Progr. Earth Planet. Sci., 8: 65.

Arai S., 1987. An estimation of the least depleted spinel peridotite on the basis of olivine-spinel mantle array. N. Jahr. Miner. Monatsh., 8: 347-354.

Arai S., 1994a. Characterization of spinel peridotites by olivine-spinel compositional relationships: Review and interpretations. Chem. Geol., 113: 191-204.

Arai S., 1994b. Chemistry of chromian spinel in volcanic rocks as a potential guide to magma chemistry. Miner. Mag., 56: 173-184.

Arai S., Matsukage K., Isobe E. and Vysotskiy S., 1997. Concentration of incompatible elements in oceanic mantle: Effect of melt/wall interaction in stagnant or failed melt conduits within peridotite. Geochim. Cosmochim. Acta, 61: 671-675.

Arai S., Tamura A., Miura M. and Morishita T., 2022. Origin of spinel-hosted mineral inclusions in mantle peridotite from Setogawa in the Circum-Izu Massif Serpentine Belt, central Japan: Implications for the chromitite genesis. Ore Geol. Rev., 140: 104422.

Asahina T. and Komatsu M., 1979. The Horokanai ophiolitic complex in the Kamuikotan Tectonic Belt, Hokkaido, Japan. J. Geol. Soc. Jap., 85: 317-330.

Barrett N., Jaques A.L., González-Álvarez I., Walter M.J. and Pearson, D.G., 2022. Ultra-refractory peridotites of Phanerozoic mantle origin: the Papua New Guinea ophiolite mantle tectonites. J. Petrol,, 63: 1-30.

Bénard A. and Ionov D.A., 2013. Melt- and fluid-rock interaction in supra-subduction lithospheric mantle: Evidence from andesite-hosted veined peridotite xenoliths. J. Petrol., 54: 2339-2378.

Birner S.K., Warren J.M., Cottrell E., Davis F.A., Kelle K.A. and Falloon T.J., 2017. Forearc peridotites from Tonga record heterogeneous oxidation of the mantle following subduction initiation. J. Petrol., 58: 1755-1780.

Bizimis M., Salters V.J.M. and Bonatti E., 2000. Trace and REE content of clinopyroxenes from supra-subduction zone peridotite. Implications for melting and enrichment processes in island arcs. Chem. Geol., 165: 67-85.

Borisova A.Y., Ceuleneer G., Kamenetsky V.S., Arai S., Béjina F., Abily B., Bindeman I.N., Polvé M., Parseval P.D., Aigouy T. and Pokrovski G.S., 2012. A new view on the petrogenesis of the Oman ophiolite chromitites from microanalyses of chromite-hosted inclusions. J. Petrol. 53: 2411-2440.

Chen J. and Zeng Z., 2007. Metasomatism of the peridotites from southern Mariana fore-arc: Trace element characteristics of clinopyroxene and amphibole. Sci. in China Series D: Earth Sci., 50: 1005-1012.

Cluzel D., Ulrich M., Jourdan F., Meffre S., Paquette J.-L., Audet M.-A., Secchiari, A. and Maurizot P., 2016. Early Eocene clinoenstatite boninite and boninite-series dikes of the ophiolite of New Caledonia; a witness of slab-derived enrichment of the mantle wedge in a nascent volcanic arc. Lithos, 260: 429-442.

D'Errico M.E., Warren J.M. and Godard M., 2016. Evidence for chemically heterogeneous Arctic mantle beneath the Gakkel Ridge. Geochim. Cosmochim. Acta, 174: 291-312.

Falloon T.J. and Danyushevsky L.V., 2000. Melting of refractory mantle at 1.5, 2 and 2.5GPa under anhydrous and H_2O-undersaturated conditions: Implications for the petrogenesis of high-Ca boninites and the influence of subduction components on mantle melting. J. Petrol., 41: 257-283.

Grégoire M., McInnes B.I.A. and O'Reilly S.Y., 2001. Hydrous metasomatism of oceanic sub-arc mantle, Lihir, Papua New Guinea: Part 2. Trace element characteristics of slab-derived fluids. Lithos, 59: 91-108.

Hawthorne F.C., Oberti R., Harlow G.E., Maresch W.V., Martin R.F., Schumacher J.C. and Welch M.D., 2012. Nomenclature of the amphibole supergroup. Am. Miner., 97: 2031-2048.

Hellebrand E., Snow J.E., Dick H.J.B. and Hofman A.W., 2001. Coupled major and trace elements as indicators of the extent of melting in mid-ocean-ridge peridotites. Nature, 410: 677-681.

Hellebrand E., Snow J.E., Mostefaoui S. and Hoppe P., 2005. Trace element distribution between orthopyroxene and clinopyroxene in peridotites from the Gakkel Ridge: a SIMS and NanoSIMS study. Contrib. Miner. Petrol., 150: 486-504.

Ichiyama Y., Tsujimori T., Fryer P., Michibayashi K., Tamura A. and Morishita T., 2021. Temporal and spatial mineralogical changes in clasts from Mariana serpentinite mud volcanoes: Cooling of the hot forearc-mantle at subduction initiation. Lithos, 384-385: 105941.

Igarashi T., Katoh T. and Niida K., 1985. The Takadomari serpentinites in the Kamuikotan ophiolite belt, Hokkaido, Japan. J. Fac. Sci., Hokkaido Univ., 21: 305-319.

Ionov D.A., 2010. Petrology of mantle eedge lithosphere: new data on supra-subduction zone peridotite xenoliths from the andesitic Avacha volcano, Kamchatka. J. Petrol., 51: 327-361.

Ishii A., Okamoto K. and Watanabe T., 2002. Finding of chromian richterite rocks from the Horokanai ophiolite. Bullb. Shibetsu City Museum, 20: 17-25 (in Japanese).

Ishii T., Robinson P.T., Maekawa H. and Fiske R., 1992. Petrologi-

cal studies of peridotites from diapiric serpentinite seamounts in the Izu-Ogasawara-Mariana forearc, LEG125. In: P. Fryer, J.A. Pearce and L.B. Stokking (Eds.), Proceed. O.D.P. Progr., Sci.. Res., 125: 445-485.

Ishikawa T., Nagahashi K. and Umino S. 2002. Boninitic volcanism in the Oman ophiolite: Implications for thermal condition during transition from spreading ridge to arc. Geology, 30: 899-902.

Ishimaru S. and Arai S., 2008. Calcic amphiboles in peridotite xenoliths from Avacha volcano, Kamchatka, and their implications for metasomatic conditions in the mantle wedge, In: M. Coltorti and M. Grégoire (Eds), Metasomatism in oceanic and continental lithospheric mantle Geol. Soc. London Spec. Publ.,293: 35-55.

Ishimaru S., Arai S., Ishida Y., Shirasaka M. and Okrugin V.M., 2007. Melting and multi-stage metasomatism in the mantle wedge beneath a frontal arc inferred from highly depleted peridotite xenoliths from the Avacha volcano, southern Kamchatka. J. Petrol., 48: 395-433.

Ishizuka H., 1980. Soda-tremolite-bearing dunite from the Horokanai ophiolite in the Kamuikotan tectonic belt, Hokkaido, Japan. J. Jap. Ass. Miner. Petrol., Econ. Geol. 75, 372-377.

Ishizuka H., 1985. Prograde metamorphism of the Horokanai ophiolite in the Kamuikotan Zone, Hokkaido, Japan. J. Petrol., 26: 391-417.

Ishizuka H., 1987. Igneous and metamorphic petrology of the Horokanai ophiolite in the Kamuikotan zone, Hokkaido, Japan: A synthetic thesis. Mem, Fac. Sci., Kochi Univ. Ser. E, Geol., 8: 1-70.

Ishizuka H., Imaizumi M., Gouchi N. and Bannno S., 1983. The Kamuikotan zone in Hokkaido, Japan: Tectonic mixing of high-pressure and low-pressure metamorphic rocks. J Metam. Geol., 1: 263-275.

Jaques A.L. and Chappell B.W., 1980. Petrology and trace element geochemistry of the Papuan ultramafic belt. Contrib. Miner. Petrol., 75: 55-75.

Jean M.M. and Shervais J.W., 2017. The distribution of fluid mobile and other incompatible trace elements in orthopyroxene from mantle wedge peridotites. Chem. Geol., 457: 118-130.

Jochum K.P. and Nohl U., 2008. Reference materials in geochemistry and environmental research and the GeoReM database. Chem. Geol., 253: 50-53.

Johnson K.T.M., Dick H.J.B. and Shimizu N., 1990. Melting in the oceanic upper mantle: an ion microprobe study of diopsides in abyssal peridotites. J. Geophys. Res., 95: 2661-2678.

Katoh T. and Nakagawa M., 1986. Tectogenesis of ultramafic rocks in the Kamuikotan tectonic belt, Hokkaido, Japan. Monogr. Ass. Geol. Collabor. Japan, 31: 119-135. (in Japanese with English abstract)

König S., Münker C., Schuth S., Luguet A., Hoffmann J.E. and Kuduon J., 2010. Boninites as windows into trace element mobility in subduction zones. Geochim. Cosmochim. Acta, 74: 684-704.

Kubo K., 2002. Dunite formation processes in highly depleted peridotite: case study of the Iwanaidake peridotite, Hokkaido, Japan. J. Petrol., 43: 423-448.

Kushiro I., 1972. Effect of water on the composition of magmas formed at high pressures. J. Petrol., 13: 311-334.

Leake B., Woolley A., Arps C., Birch W., Gilbert C., Grice J., Hawthorne F., Kato A., Kisch, H., Vladimir K., Linthout K., Laird J., Mandarino J., Maresch W., Nickel E., Rock N., Schumacher J., Smith D., Stephenson N. and Guo Y., 1997. Nomenclature of amphiboles; Report of the Subcommittee on Amphiboles of the International Mineralogical Association, Commission on New Minerals and Mineral Names. Am. Miner., 82: 1019-1037.

Le Roux V., Dick H.J.B. and Shimizu N., 2014. Tracking flux melting and melt percolation in supra-subduction peridotites (Josephine ophiolite, USA). Contrib. Miner. Petrol., 168: 1-22.

Li Y.-B., Kimura J.-I., Machida S., Ishii T., Ishiwatari A., Maruyama S., Qiu H.-N., Ishikawa T., Kato Y., Haraguchi S., Takahta N., Hirahaa Y. and Miyazaki T., 2013. High-Mg adakite and Low-Ca boninite from a Bonin fore-arc seamount: implications for the reaction between slab melts and depleted mantle. J. Petrol., 54: 1149-1175.

Locock A.J., 2014. An Excel spreadsheet to classify chemical analyses of amphiboles following the IMA 2012 recommendations. Comput. Geosci., 62: 1-11.

Longerich H.P., Jackson S.E. and Gunther D., 1996. Laser ablation inductively coupled plasma mass spectrometric transient signal data acquisition and analyte concentration calculation. J. Analyt. Atomic Spectr., 11: 899-904.

Maulana A., Christy A.G., Ellis D.J. and Bröcker M., 2019. The distinctive tectonic and metamorphic history of the Barru Block, South Sulawesi, Indonesia: Petrological, geochemical and geochronological evidence. J. Asian Earth Sci., 172: 170-189.

Morishita T., Ishida Y. and Arai S., 2005. Simultaneous determination of multiple trace element compositions in thin (< 30μm) layers of BCR-2G by 193 nm ArF excimer laser ablation-ICP-MS: implications for matrix effect and elemental fractionation on quantitative analysis. Geochem. J., 39: 327-340.

Morishita T., Tani K., Shukuno H., Harigane Y., Tamura A., Kumagai H. and Hellebrand E., 2011. Diversity of melt conduits in the Izu-Bonin-Mariana forearc mantle: Implications for the earliest stage of arc magmatism. Geology, 39: 411-414.

Nishio I., Morishita T., Tamura A., Itano K., Takamizawa S., Ichiyama Y., Arai S., Barrett N. and Szilas K., 2023. Formation of ultra-depleted mantle peridotites and their relationship with boninitic melts: an example from the Kamuikotan unit, Hokkaido, Japan. J. Geophys. Res. Solid Earth, 128: e2022JB025066.

Ohara Y. and Ishii T., 1998. Peridotites from the southern Mariana forearc: Heterogeneous fluid supply in mantle wedge. Isl. Arc, 7: 541-558.

Ozawa K., 1988. Ultramafic tectonite of the Miyamori ophiolitic complex in the Kitakami Mountains, Northeast Japan: hydrous upper mantle in an island arc. Contrib. Miner. Petrol., 99: 159-175.

Ozawa K., 2001. Mass balance equations for open magmatic systems: trace element behavior and its application to open system melting in the upper mantle. J. Geophys. Res., 106: 13407-13434.

Parkinson I.J. and Pearce J.A., 1998. Peridotites from the Izu-Bonin-Mariana forearc (ODP Leg 125): evidence for mantle melting and melt-mantle interaction in a supra-subduction zone setting. J. Petrol., 39: 1577-1618.

Parkinson I.J., Pearce J.A., Thirlwall M.F., Johnson K.T.M. and Ingram G., 1992. Trace element geochemistry of peridotites from the Izu-Bonin-Mariana forearc. Proc. O.D.P., Sci. Res., 125: 487-506.

Pearce J.A., van der Laan S.R., Arculus R.J., Murton B.J., Ishii T., Peate D.W. and Parkinson I.J., 1992. Boninite and harzburgite from LEG 125 (Bonin-Mriana Forearc): a case study of magma genesis during the initial stages of subduction, In: P.F Fryer, J.A. Pearce and L.B. Stokking (Eds.), Prooceed, O. D. P. Sci, Res. 125: 623-657.

Prouteau G., Scaillet B., Pichavant M. and Maury R., 2001. Evidence for mantle metasomatism by hydrous silicic melts derived from subducted oceanic crust. Nature, 410: 197-200.

Qiao J., Dong J., Song S., Wang C., Allen M.B. and Su L., 2022. Melting of mafic slab and mantle peridotite during ridge subduction of the Proto-Tethys Ocean (Qilian Orogen, NW China). Lithos, 410-411: 106588.

Sakakibara M. and Ota T., 1994. Metamorphic evolution of the Kamuikotan high-pressure and low-temperature metamorphic rocks in central Hokkaido, Japan. J. Geophys. Res. Solid Earth, 99: 22221-22235.

Scott J.M., Liu J., Pearson D.G. and Waight T.E., 2016. Mantle depletion and metasomatism recorded in orthopyroxene in highly depleted peridotites. Chem. Geol., 441: 280-291.

Secchiari A., Montanini A., Bosch D., Macera P. and Cluzel D., 2020. Sr, Nd, Pb and trace element systematics of the New Caledonia harzburgites: Tracking source depletion and contamination processes in a SSZ setting. Geosci., Front., 11: 37-55.

Seyler M. and Brunelli D., 2018. Sodium chromium covariation in residual clinopyroxenes from abyssal peridotites sampled in the 43°-46°E region of the Southwest Indian Ridge. Lithos, 302-303: 142-157.

Seyler M., Brunelli D., Toplis M.J. and Mével C., 2011. Multiscale chemical heterogeneities beneath the eastern Southwest Indian Ridge (52°E-68°E): Trace element compositions of along-axis dredged peridotites. Geochem. Geophys. Geosyst., 12: Q0AC15.

Shimizu K., Liang Y., Sun C., Jackson C.R.M. and Saal A.E., 2017. Parameterized lattice strain models for REE partitioning between amphibole and silicate melt. Am. Miner., 102: 2254-2267.

Suhr G., Hellebrand E., Snow J.E., Seck H.A. and Hofman A.W., 2003. Significance of large, refractory dunite bodies in the upper mantle of the Bay of Islands Ophiolite. Geochem. Geophys. Geosyst., 4: 8605.

Sun S.S. and McDonough W.F., 1989. Chemical and isotopic systematics of oceanic basalts: implications for mantle composition and processes, In: A.D. Saunders and M.J. Norry (Eds.), Magmatism in the Ocean Basins. Geol. Soc. London Spec. Publ., 42: 313-345.

Tamura A. and Arai S., 2005. Unmixed spinel in chromitite from the Iwanai-dake peridotite complex, Hokkaido, Japan: a reaction between peridotite and highly oxidized magma in the mantle wedge. Am. Miner.t, 90: 473-480.

Tamura A. and Arai S., 2006a. Harzburgite-dunite-orthopyroxenite suite as a record of supra-subduction zone setting for the Oman ophiolite mantle. Lithos, 90: 43-56.

Tamura A. and Arai S., 2006b. Geochemistry of clinopyroxene in peridotites from the Nukabira complex, Kamuikotan zone, Hokkaido, Japan: a LA-ICP-MS study. Sci. Rep. Kanazawa Univ., 50: 1-27.

Tamur A., Arai S., Ishimaru S. and Andal E., 2008. Petrology and geochemistry of peridotites from IODP Site U1309 at Atlantis Massif, MAR 30°N: micro- and macro-scale melt penetrations into peridotites. Contrib. Miner. Petrol., 155: 491-509.

Tamura A., Makta, M. and Arai S., 1999a. Origin of highly refractory peridotites: implications for diversity of high-Mg andesite magma genesis. Abstract for 3rd Intern. Workshop on Orogenic Lherzolite and Mantle Processes. Ofioliti, 24: 174-175.

Tamura A., Makita M. and Arai S., 1999b. Petrogenesis of ultramafic rocks in the Kamuikotan belt, Hokkaido, northern Japan. Mem. Geol. Soc. Jap., 52: 53-68. (in Japanese with English abstract)

Tamura A., Morishita T., Ishimaru S. and Arai S., 2014. Geochemistry of spinel-hosted amphibole inclusions in abyssal peridotite: insight into secondary melt formation in melt-peridotite reaction. Contrib. Miner. Petrol., 167: 1-16.

Tamura A., Morishita T., Ishimaru S., Hara K., Sanfilippo A. and Arai S., 2016. Compositional variations in spinel-hosted pargasite inclusions in the olivine-rich rock from the oceanic crust–mantle boundary zone. Contrib. Miner. Petrol., 171: 1-14.

Tamura A., Sagawa T., Okino K. and Morishita T., 2022. Determination of whole-rock trace-element compositions of siliceous rocks using MgO-diluted fused glass and LA-ICP-MS. Geochem. J., 56: 231-239.

Tatsumi Y., Sakuyama M., Fukuyama H. and Kushiro I., 1983. Generation of arc basalt magmas and thermal structure of the mantle wedge in subduction zones. J. Geophys. Res. Solid Earth, 88: 5815-5825.

Umino S. and Kushiro I., 1989. Experimental studies on boninite petrogenesis, In: A.J. Crawford (Ed.), Boninites and related rocks. Unwin Hyman, London, p. 89-111.

Umino S., Kitamura K., Kanayama K., Tamura A., Sakamoto N., Ishizuka O. and Arai S., 2015. Thermal and chemical evolution of the subarc mantle revealed by spinel-hosted melt inclusions in boninite from the Ogasawara (bonin) Archipelago, Japan. Geology, 43: 151-154.

Umino S., Kanayama K., Kitamura K., Tamura A., Ishizuka O., Senda R. and Arai S., 2018. Did boninite originate from the heterogeneous mantle with recycled ancient slab. Island Arc, 27: e12221.

Varfalvy V., Hébert R. and Bédard J.H., 1996. Interactions between melt and upper-mantle peridotites in the North Arm Mountain massif, Bay of Islands ophiolite, Newfoundland, Canada: Implications for the genesis of boninitic and related magmas. Chem. Geol., 129: 71-90.

Wallis S.R., Yamaoka K., Mori H., Ishiwatari A., Miyazaki K. and Ueda H., 2020. The basement geology of Japan from A to Z. Isl, Arc, 29: e12339.

Warren J.M., 2016. Global variations in abyssal peridotite compositions. Lithos, 248-251: 193-219.

Xu Y., Liu C.-Z. and Lin W., 2021. Melt extraction and reaction in the forearc mantle: Constraints from trace elements and isotope geochemistry of ultra-refractory peridotites of the New Caledonia Peridotite Nappe. Lithos, 380-381: 105882.

Zanetti A., Mazzucchelli M., Rivalenti G. and Vannucci R., 1999. The Finero phlogopite-peridotite massif: an example of subduction-related metasomatism. Contrib. Miner. Petrol., 134: 107-122.

Received, November 6, 2023
Accepted, December 28, 2023